Parallel Solution-Adaptive Method for Two-Dimensional Non-Premixed Combusting Flows

X. Gao*[1], S. Northrup[2], and C. P. T. Groth[2]
[1] MS 50A-1148, Lawrence Berkeley National Lab
1 Cyclotron Rd., Berkeley, CA 94720, USA
[2] Institute for Aerospace Studies
University of Toronto
4925 Dufferin Street, Toronto, ON M3H 5T6, Canada
E-mail and Fax:
XinfengGao@lbl.gov, Fax: 1 (510)4866900
northrup@utias.utoronto.ca
groth@utias.utoronto.ca
*Corresponding author

Abstract: A parallel adaptive mesh refinement (AMR) algorithm is proposed and applied to the predictions of both laminar and turbulent steady non-premixed compressible combusting flows. The parallel solution-adaptive algorithm solves the system of partial-differential equations governing two-dimensional axisymmetric laminar and turbulent compressible flows for reactive thermally perfect gaseous mixtures using a fully coupled finite-volume formulation on body-fitted multi-block quadrilateral mesh. The compressible formulation can readily accommodate large density variations and thermo-acoustic phenomena. A local preconditioning technique is used to remove numerical stiffness and maintain solution accuracy for low-Mach-number, nearly-incompressible flows. A preconditioned multigrid algorithm is used for the efficient solution on highly stretched meshes. A flexible block-based hierarchical data structure is used to maintain the connectivity of the solution blocks in the multi-block mesh and facilitate automatic solution-directed mesh adaptation according to physics-based refinement criteria. This AMR approach allows for anisotropic mesh refinement and the block-based data structure readily permits efficient and scalable implementations of the algorithm on multi-processor architectures. For calculations of near-wall turbulence, an automatic near-wall treatment readily accommodates situations during adaptive mesh refinement where the mesh resolution may not be sufficient for directly calculating near-wall turbulence using the low-Reynolds-number formulation. Numerical results for co-flow laminar and turbulent diffusion flames are described and compared to available experimental data. The numerical results demonstrate the validity and potential of the parallel AMR approach for predicting both fine-scale features of laminar and complex turbulent non-premixed flames.

Keywords: parallel solution-adaptive algorithm; adaptive mesh refinement; laminar combustion; turbulent combustion; non-premixed flames; diffusion flames.

Reference to this paper should be made as follows: Gao, X., Northrup, S. and Groth, C. P. T. (2010) 'Parallel solution-adaptive method for two-dimensional non-premixed combusting flows', *Progress in Computational Fluid Dynamics*

Biographical notes: Xinfeng Gao obtained a M.S. degree in Aerospace Engineering from Syracuse University, USA and a Ph.D. degree in Aerospace Science and Engineering from University of Toronto. She is currently a postdoctoral researcher at Lawrence Berkeley National Lab in USA. Scott Northrup is a Ph.D. candidate at the Institute for Aerospace Studies, University of Toronto. Clinton P. T. Groth is a Professor at the Institute for Aerospace Studies, University of Toronto, Toronto, Canada.

1 INTRODUCTION

In the last twenty years, numerical methods have become an essential tool for the investigation of combusting flows. The application of computational fluid dynamics (CFD) methods to reactive flows has yielded an improved understanding of combustion processes. Nevertheless, combustion involves a wide range of complicated physical and chemical phenomena(flame behaviour is dictated by a strong interaction between the flow structure, chemical kinetics, and thermodynamic properties of the reactants and products), each with their own characteristic spatial and/or temporal scales. In many cases, combusting flows exhibit large disparities in these characteristic scales, mainly because combustion is usually associated with turbulent flows. Due to more manageable computational requirements and somewhat greater ease in handling complex flow geometries, most practical simulation algorithms are based on the Reynolds- or Favre-averaged Navier-Stokes equations, where the turbulent flow structure is entirely modelled and not resolved. In spite of simplifications offered by the time-averaging approach, the system of equations governing combusting flows can be both large and stiff and its solution can still place severe demands on available computational resources.

Many approaches have been taken to reduce the computational costs of simulating combusting flows. One successful approach is to make use of solution-directed mesh adaptation, such as the adaptive mesh refinement algorithms developed for aerospace applications (Berger (1984); Berger and Colella (1989); Quirk (1991); Powell et al. (1993); De Zeeuw and Powell (1993); Quirk and Hanebutte (1993); Berger and Saltzman (1994); Aftosmis (1998); Groth et al. (1999, 2000)). Computational grids that automatically adapt to the solution of the governing equations are very effective in treating problems with disparate length scales, providing the required spatial resolution while minimising memory and storage requirements. Recent progress in the development and application of AMR algorithms for low-Mach-number reacting flows and premixed turbulent combustion is described by Day and Bell (2000) and Bell et al. (2001, 2002). Another approach for coping with the computational cost of reacting flow prediction is to apply a domain decomposition procedure and solve the problem in a parallel fashion using multiple processors. Large massively parallel distributed-memory computers can provide many fold increases in processing power and memory resources beyond those of conventional single-processor computers and would therefore provide an obvious avenue for greatly reducing the time required to obtain numerical solutions of combusting flows.

This work seeks to combine these two numerical approaches, producing a parallel AMR method that both reduces the overall problem size and the time to calculate steady solutions for combusting flows from the laminar to turbulent regimes. In particular, a highly scalable parallel block-based AMR algorithm is proposed for predicting a wide range of two-dimensional non-premixed compressible combusting flows.

In the following sections, the mathematical modelling of non-premixed combustion is presented for turbulent flows and the parallel AMR algorithm is described in details. Numerical verification of the proposed parallel AMR scheme is then presented by considering the numerical predictions for three classical non-reacting flow problems and one reactive flow problem. Numerical results are described and discussed for non-premixed methane-air laminar and turbulent co-flow axisymmetric diffusion flames. Finally, conclusions of this work are given.

2 MATHEMATICAL MODELLING

The governing conservation equations describing the behaviour of a thermally perfect compressible reactive gaseous mixture are formulated for both laminar and turbulent reactive flows. For laminar reactive flows, Navier-Stokes equations are employed and the formulation is rather standard and straightforward. Herein, we will only present mathematical modelling for turbulent combusting flows to keep this section brief.

2.1 Favre-Averaged Navier-Stokes Equations

A system of Favre-averaged Navier-Stokes equations describing a thermally-perfect compressible turbulent reactive mixture can be formulated as:

$$\frac{\partial \rho}{\partial t} + \vec{\nabla}\cdot(\rho\vec{u}) = 0\,, \tag{1}$$

$$\frac{\partial}{\partial t}(\rho\vec{u}) + \vec{\nabla}\cdot\left(\rho\vec{u}\vec{u} + p\vec{\vec{I}}\right) = \vec{\nabla}\cdot\left(\vec{\vec{\tau}} + \vec{\vec{\lambda}}\right)\,, \tag{2}$$

$$\begin{aligned}\frac{\partial}{\partial t}(\rho e) + \vec{\nabla}\cdot\left[\rho\vec{u}\left(e + \frac{p}{\rho}\right)\right] = {} & \vec{\nabla}\cdot\left[\left(\vec{\vec{\tau}} + \vec{\vec{\lambda}}\right)\cdot\vec{u}\right] + \\ & \vec{\nabla}\cdot\left(D_k\vec{\nabla}k\right) - \vec{\nabla}\cdot\left(\vec{q} + \vec{q}_t\right)\,,\end{aligned} \tag{3}$$

$$\frac{\partial}{\partial t}(\rho c_n) + \vec{\nabla}\cdot(\rho c_n\vec{u}) = -\vec{\nabla}\cdot\left(\vec{J}_n + \vec{J}_{tn}\right) + \rho\dot{w}_n\,, \tag{4}$$

where Eqs. (1)–(3) reflect the conservation of mass, momentum, and energy for the reactive mixture, ρ is the Reynolds-averaged mixture density, $\vec{u}$ is the Favre-averaged mean velocity of the mixture, p is the Reynolds-averaged mixture pressure given by the ideal gas law $p = \sum_{n=1}^{N} \rho c_n R_n T$ where N is the number of species, R_n is the species gas constant, and T is the mixture temperature. Here, $e = |\vec{u}|^2/2 + \sum_{n=1}^{N} c_n h_n - p/\rho + k$ is the Favre-averaged total specific mixture energy, k is the specific turbulent kinetic energy and D_k is the coefficient for the diffusion of the turbulent energy, $\vec{\vec{\tau}}$ and $\vec{\vec{\lambda}}$ are the fluid stress tensor and the turbulent Reynolds stress tensor for the mixture, respectively, $\vec{q}$ and $\vec{q}_t$ are the laminar and turbulent heat flux vector, respectively. Eq. (4) describes

Copyright © 200x Inderscience Enterprises Ltd.

the time evolution of the species mass fraction, where $\dot{w}_n$ is the time-averaged or mean rate of the change of the species mass fraction produced by the chemical reactions. The molecular stress is given by the general stress-strain relationship $\vec{\vec{\tau}} = 2\mu(\vec{\vec{S}} - \frac{1}{3}\vec{\vec{I}}\vec{\nabla}\cdot\vec{u})$, where μ is molecular viscosity, $\vec{\vec{S}}$ is the strain rate tensor, and $\vec{\vec{I}}$ is the identity tensor. For species n, the molecular and turbulent diffusive flux, $\vec{\mathcal{J}}_n$ and $\vec{\mathcal{J}}_{tn}$, are modelled by

$$\vec{\mathcal{J}}_{ln} = -\rho D_n \nabla c_n \quad \text{and} \quad \vec{\mathcal{J}}_{tn} = -\rho D_{t_n} \nabla c_n \,.$$

The molecular and turbulent heat flux are modelled by

$$\vec{q} = -\left(\kappa\nabla T - \sum_{n=1}^{N} h_n \vec{\mathcal{J}}_n\right) \text{ and } \vec{q}_t = -\left(\kappa_t\nabla T - \sum_{n=1}^{N} h_n \vec{\mathcal{J}}_{tn}\right) ,$$

where κ and κ_t are the laminar and turbulent thermal conductivity of the mixture and D_n and D_{t_n} are the molecular and turbulent diffusivity of species n relative to the major species, respectively. Given laminar and turbulent Schmidt numbers, Sc and Sc_t, D_n and D_{t_n} are obtained using $D_n = \mu/\rho Sc$ and $D_{t_n} = \mu_t/\rho Sc_t$. In addition, h_n is the absolute (chemical and sensible) internal enthalpy for species n.

2.2 Two-Equation k-ω Model

The two-equation k-ω model of Wilcox (1998) is used here to model the unresolved turbulent flow quantities. In this approach, the Boussinesq approximation is used to relate the Reynolds stress tensor, $\vec{\vec{\lambda}}$, to the mean flow strain-rate tensor using a turbulent eddy viscosity, μ_t, $\vec{\vec{\lambda}} = 2\mu_t(\vec{\vec{S}} - \frac{1}{3}\vec{\vec{I}}\vec{\nabla}\cdot\vec{u}) - \frac{2}{3}\vec{\vec{I}}\rho k$ with $\mu_t = \rho k/\omega$. Transport equations are solved for turbulent kinetic energy, k, and the specific dissipation rate, ω, given by

$$\frac{\partial}{\partial t}(\rho k) + \vec{\nabla}\cdot(\rho k\vec{u}) = \vec{\vec{\lambda}} : \vec{\nabla}\vec{u} + \vec{\nabla}\cdot\Big[\left(\mu + \mu_t\sigma^*\right)\vec{\nabla}k\Big] - \beta^*\rho k\omega \,, \tag{5}$$

$$\frac{\partial}{\partial t}(\rho\omega) + \vec{\nabla}\cdot(\rho\omega\vec{u}) = \alpha\frac{\omega}{k}\vec{\vec{\lambda}} : \vec{\nabla}\vec{u} + \vec{\nabla}\cdot\Big[\left(\mu + \mu_t\sigma\right)\vec{\nabla}\omega\Big] - \beta\rho\omega^2 \,, \tag{6}$$

where σ^*, β^*, α, σ, and β are closure coefficients for the two-equation model and are given by Wilcox (2002).

2.3 Thermodynamic and Transport Properties

Thermodynamic relationships and transport coefficients are required to close the systems of equations given above for both laminar and turbulent combusting flows. Thermodynamic and molecular transport properties of each gaseous species are prescribed using the empirical database compiled by Gordon and McBride (1994) and McBride and Gordon (1996), which provides curve fits for the species enthalpy, h_n; specific heat, c_{p_n}; entropy; viscosity, μ_n; and thermal conductivity, κ_n, as functions of temperature, T. The Gordon-McBride data set contains curve fits for over 2000 substances, including 50 reference elements.

The molecular viscosity, μ, and thermal conductivity, κ, of the reactive mixture are determined using the mixture rules of Wilke (1950) and Mason and Saxena (1958), respectively. Turbulent contributions to thermal conductivity and species diffusivity are modelled by making an analogy between momentum and heat and mass transfer and introducing the turbulent Prandtl and Schmidt numbers, Pr_t and Sc_t, both of which are taken to be constant ($\text{Pr}_t = 0.9$ and $\text{Sc}_t = 1$), and assuming $\kappa_t = \mu_t c_p/\text{Pr}_t$ and $D_{tn} = \mu_t/\rho\text{Sc}_t$.

2.4 Reduced Chemical Kinetics

The combustion of methane is considered here. Although several detailed chemical reaction mechanisms are available for describing methane-air combustion processes (GRI-Mech 3.0), for computational simplicity, our attention shall be restricted to reduced chemical kinetic schemes. Both one- and two-step reduced chemical reaction mechanisms as described by Westbrook and Dryer (1981) are used.

Empirically derived expressions for the reaction rates in each case are used. The five species considered in the one-step reaction mechanism are methane (CH_4), oxygen(O_2), carbon dioxide (CO_2), water (H_2O), and nitrogen (N_2). Nitrogen is assumed to be inert. Carbon monoxide (CO) species is also considered in the two-step reaction mechanism. Further details and reaction rates for these reduced mechanisms are given by Westbrook and Dryer (1981).

2.5 Eddy Dissipation Model

The mean reaction rates, $\dot{\omega}_\text{n}$, in Eq. (4) describe the mean production and consumption of each of the chemical species due to the chemical reactions and strong interactions between turbulence and chemistry and are estimated using the eddy dissipation model (EDM) of Magnussen and Hjertager (1976). This model assumes that turbulence mixing limits the fuel burning and that the fuel reaction rate is limited by the deficient species. The individual species mean reaction rate is then taken to be the minimum of the rates given by the finite-rate chemical kinetics (i.e., the law of mass action and Arrhenius reaction rates) and the EDM value. The latter is related to the turbulence mixing time and is estimated using the dissipation rate, ω.

2.6 Treatment of Near-Wall Turbulence

Both low-Reynolds-number and wall-function formulations of the k-ω model are used for the treatment of near-wall turbulent flows, with a procedure for automatically switching from one to the other, depending on mesh resolution. In the case of the low-Reynolds-number formulation, it can be shown that $\lim_{y\to 0}\omega = \frac{6\nu}{\beta_o y^2}$ where y is the distance normal from the wall. Rather than attempting to solve the ω-equation directly, the preceding expression is used to specify ω for all values of $y^+ \leq 2.5$, where $y^+ = u_\tau y/\nu$, $u_\tau^2 = \tau_w/\rho$, and τ_w is the wall shear stress. Provided there are 3–5 computational cells inside $y^+ = 2.5$, this procedure reduces numerical stiffness, guarantees numerical accuracy, and permits the k-ω model to be solved directly in the near-wall region without resorting to wall functions. In the case of the wall-function formulation, the expressions $k = \frac{u_\tau^2}{\sqrt{\beta_o^*}}$, $\omega = \frac{u_\tau}{\sqrt{\beta_o^*}\kappa y}$, are used to fully specify k and ω for $y^+ \leq$30-250, where κ is the von Kármán constant.

A procedure has also been developed to automatically switch between these two approaches, depending on the near-wall mesh resolution. In this procedure, the values of k and ω are approximated by

$$k = \frac{u_\tau^2}{\sqrt{\beta_o^\star}} \left(\frac{\min(\mathrm{y}^+, 30)}{30} \right)^2 \quad \text{and } \omega = \omega_\mathrm{o} \sqrt{1 + \left(\frac{\omega_\mathrm{wall}}{\omega_\mathrm{o}} \right)^2} \,,$$

where $\omega_\mathrm{o} = \frac{6\nu}{\beta_o y^2}$ and $\omega_\mathrm{wall} = \frac{u_\tau}{\sqrt{\beta^*}\kappa y}$. This procedure has been devised to prescribe k and ω for y^+ lying between 2.5 and a cutoff value. where ω_o and ω_wall are the values in the near-wall sub-layer and in the log layer, respectively. The cutoff is taken to be in the range 30–50 for this study. When y^+ is close to the lower limit, 2.5, k and ω approach zero and the asymptotic value, respectively. When y^+ approaches the cutoff value, the wall function is recovered. This automatic near-wall treatment readily accommodates situations during adaptive mesh refinement where the mesh resolution may not be sufficient for directly calculating near-wall turbulence using the low-Reynolds-number formulation.

3 PARALLEL AMR ALGORITHM

3.1 Finite Volume Scheme

A finite volume scheme is proposed to solve the system of partial-differential equations governing two-dimensional axisymmetric laminar and turbulent compressible flows for reactive thermally perfect gaseous mixtures using a fully coupled finite-volume formulation on body-fitted multi-block quadrilateral mesh. Applying the divergence theorem to the differential form of the system of governing equations in two-dimensional axisymmetric coordinates, Eqs. (1)–(6)), one arrives at the integral form

$$\frac{d}{dt} \int_{A(t)} \mathbf{U} dA + \oint_{l(t)} \vec{n} \cdot \vec{\mathbf{F}} \, dl = \int_{A(t)} \left(-\frac{\mathbf{S}_a}{r} + \mathbf{S_c} + \mathbf{S_t} \right) dA \,, \quad (7)$$

where $\mathbf{U}$ is the vector of conserved variables, $\vec{\mathbf{F}}$ the flux dyad, defined as $\vec{\mathbf{F}} = (\mathbf{F} - \mathbf{F}_v, \mathbf{G} - \mathbf{G}_v)$, $\mathbf{S}_a$ the source term associated with the axisymmetric geometry, $\mathbf{S_c}$ and $\mathbf{S_t}$ the source terms due to finite rate chemistry and turbulence modelling to be included for turbulent flows, A the control area, l the closed contour of the control volume, r is the radial distance, and $\vec{n}$ is the unit outward vector normal to the closed surface. For laminar flows, $\mathbf{U}$ is given by

$$\mathbf{U} = \left[\; \rho, \; \rho v_r, \; \rho v_z, \; \rho e, \; \rho c_1, \; \ldots, \; \rho c_N \; \right]^T \,, \quad (8)$$

and ρk and $\rho\omega$ are included for turbulent flows. Note that the last species N is chosen to be Nitrogen and used to accommodate the numerical errors. In other words, the concentration of Nitrogen is corrected by using $c_N = 1.0 - \sum_{n=1}^{N-1} c_n$ after solving the system.

This fully compressible formulation can readily accommodate large density variations and thermo-acoustic phenomena. Nevertheless, laminar combusting flows are in general characterised by very low Mach numbers ($M < 0.2$) and nearly incompressible behaviour. Therefore, a local preconditioning technique proposed by Weiss and Smith (1995) and Turkel (1999) is used here to remove numerical stiffness and maintain solution accuracy for low-Mach-number flows. The preconditioned system of governing equations is integrated over quadrilateral cells of a structured multi-block quadrilateral mesh. The semi-discrete form of this finite-volume formulation applied to cell (i, j) is given by

$$\mathbf{\Gamma} \frac{d\mathbf{U}_{i,j}}{dt} = -\frac{1}{A_{i,j}} \sum_{\mathrm{faces},k} \vec{\mathbf{F}}_{i,j,k} \cdot \vec{n}_{i,j,k} \Delta\ell_{i,j,k} - \frac{\mathbf{S}_{a\,i,j}}{r_{i,j}} + \mathbf{S}_{\mathbf{c}\,i,j} \,, \quad (9)$$

where $\mathbf{\Gamma}$ is the Weiss-Smith preconditioning matrix for the conserved variable system, $r_{i,j}$ and $A_{i,j}$ are the radial distance and area of cell (i, j), and $\Delta\ell$ is the length of the cell face.

The inviscid (hyperbolic) component of the numerical flux at each cell face is evaluated using limited linear reconstruction (Barth (1993)) and one of several Riemann-solver based flux functions (Roe (1981); Einfeldt (1988); Linde (2002)). The viscous (elliptic) component of the numerical flux is evaluated by employing a diamond-path reconstruction procedure as described by Coirier and Powell (1996).

3.2 Time Marching Method

For the time-invariant calculations performed as part of this study, a multi-stage time-marching scheme is used to solve the coupled set of non-linear ODEs, that arise from the finite-volume spatial discretisation procedure. The time-marching scheme is based on the optimally-smoothing multi-stage time marching scheme developed by van Leer et al. (1989). The general M stage optimally smoothing time-marching scheme for integrating Equation(9) from the time level n to time level $n+1$ can be written as

$$\text{m stage:} \begin{cases} \mathbf{U}^0_{i,j} = \mathbf{U}^\mathrm{n}_{i,j} \\ \mathbf{U}^\mathrm{m}_{i,j} = \mathbf{U}^0_{i,j} - \alpha_\mathrm{m} \Delta t^\mathrm{n} \, \mathbf{R}_{i,j}(\mathbf{U}^{\mathrm{m}-1}) \\ \mathbf{U}^{\mathrm{n}+1}_{i,j} = \mathbf{U}^\mathrm{M}_{i,j} \end{cases} ,$$

where $\mathrm{m} = 1 \cdots \mathrm{M}$, $\Delta t^\mathrm{n} = t^{\mathrm{n}+1} - t^\mathrm{n}$ is the size of the time step and α_m are multi-stage coefficients. The coefficients used here have been selected to optimize the high-frequency damping for first- and second-order upwind discretisations of the scalar advection equation in multigrid applications van Leer et al. (1989). They are not optimized for diffusion problems or viscous flows.

The source terms associated with finite-rate chemistry and turbulence modelling are usually responsible for much of the numerical stiffness in the resulting discretised system of equations. The use of semi-implicit time integration can be utilised to cope with the stiffness of the system. This method treats source terms implicitly, while treating the fluxes explicitly. Hence, this method avoids solving the large block matrices associated with the fully implicit scheme. A local linear system of equations is then solved to obtain the solution change using a dense matrix solver. In this case a LU decomposition was used.

The inviscid Courant-Friedrichs-Lewy stability, viscous von Neumann stability, and turbulent and chemical time step constraints are imposed when selecting the time step. Note that, for reacting flows, the inverse of the maximum diagonal of the chemical source term Jacobian is added to the time step calculation. The time step, Δt^{n}, is then determined by

$$\Delta t^{\mathrm{n}} = \min\left(\mathrm{CFL}\frac{\Delta l}{|\vec{u}|+c}, \frac{\alpha}{2}\frac{\rho \Delta l^2}{\max(\mu, \mu_{\mathrm{t}})}, \left(\beta \max(\frac{\partial \mathbf{S}_{\mathrm{c}}}{\partial \mathbf{U}})\right)^{-1}\right) \tag{10}$$

where Δl is the cell-face length of a cell, c is the sound speed, and μ and μ_{t} are molecular viscosity and turbulent eddy viscosity, respectively, and where α and β are scaling factors.

3.3 Preconditioned Multigrid

Application of multigrid to the Favre-averaged Navier-Stokes equations can result in convergence rates that are far from optimal due to the stiff source term associated with the turbulence models. Classic multigrid remedies for these multigrid difficulties, such as directional-coarsening, directional implicit smoother, combining directional coarsening and smoothing, and combining a point-implicit block-Jacobi preconditioner and J-coarsening, etc., are well documented and the effects are illustrated for some example problems by Pierce and Giles (1996, 1997) and Mavriplis (1998). Sheffer et al. (1998) employed the point-implicit formulation of Bussing and Murman (1987, 1988) in combination with an explicit time-stepping multigrid solver for calculating high speed reactive flows. Gerlinger and Brüggemann (1997) and Gerlinger et al. (1998) investigated the q-ω model and proposed the techniques of computing the production term and the divergence of velocity field only on the finest mesh and restricted these values to coarser meshes. For complicated geometries and simple flow field initializations, they initiated the calculation with several fine mesh iterations before restricting to coarser meshes. Refer Gao (2008) for details on a literature review in terms of multigrid applications to turbulent flows.

In this study, to remedy the multigrid difficulties in stability and convergence due to the stiff turbulence production terms and chemical source terms and the use of highly stretched meshes, we employed a point-implicit block-Jacobi preconditioner (matrix preconditioner) in combination with the multigrid solver. The turbulence quantities are restricted to the coarse mesh but not updated so as to enhance the stability of the scheme and avoid non-physical solutions. Note that we do not believe that the point-Jacobi preconditioning will provide a fully satisfactory solution to issues with high-aspect-ratio meshes; however, our experiences show that the preconditioning combined with modifications to the restriction and prolongation operators partially alleviates the problem.

3.3.1 Smoothing Operator

The point-implicit block-Jacobi preconditioner used herein is based on the form of the discrete residual operator, $\mathbf{R}$, and obtained by extracting the terms corresponding to the center cell in the stencil. The application of the matrix preconditioner to the multi-stage time-marching scheme is rewritten as

$$\text{m stage:} \begin{cases} \mathbf{U}^{0}_{i,j} = \mathbf{U}^{\mathrm{n}}_{i,j} \\ \mathbf{U}^{\mathrm{m}}_{i,j} = \mathbf{U}^{0}_{i,j} - \nu \alpha_{\mathrm{m}}\ \mathbf{P}^{-1}_{i,j}\ \mathbf{R}_{i,j}\ (\mathbf{U}^{\mathrm{m}-1}) \\ \mathbf{U}^{\mathrm{n}+1}_{i,j} = \mathbf{U}^{\mathrm{M}}_{i,j} \end{cases}$$

where ν includes the time step and $\mathbf{P}^{-1}_{i,j}$ is the inverse of the matrix preconditioner for cell (i,j). The construction of the matrix preconditioner is illustrated here using the system of governing equations in a two-dimensional axisymmetric system. Given the residual function for cell (i,j), $\mathbf{R}_{i,j}$, which can be written as

$$\mathbf{R}_{i,j} = \frac{d\mathbf{U}_{i,j}}{dt} = \frac{-1}{A_{\mathrm{i,j}}}\sum_{k=1}^{N_{\mathrm{f}}} \vec{\mathbf{F}}_{\mathrm{k}} \cdot \vec{n}_{\mathrm{k}}\ \Delta l_{\mathrm{k}} - \frac{\mathcal{S}_{\mathrm{a}i,j}}{r} + \mathbf{S}_{\mathrm{t}i,j} + \mathbf{S}_{\mathrm{c}i,j}, \tag{11}$$

the matrix preconditioner, $\mathbf{P}_{i,j} = \frac{\partial \mathbf{R}}{\partial \mathbf{U}}\big|_{i,j}$, is a N×N matrix and has the form

$$\mathbf{P}_{i,j} = \frac{\partial \mathbf{R}_{i,j}(\mathbf{U}, \nabla \mathbf{U})}{\partial \mathbf{U}_{i,j}} = \begin{bmatrix} \frac{\partial \mathrm{R}_1}{\partial \mathrm{U}_1} & \frac{\partial \mathrm{R}_1}{\partial \mathrm{U}_2} & \cdots & \frac{\partial \mathrm{R}_1}{\partial \mathrm{U}_{\mathrm{N}}} \\ \frac{\partial \mathrm{R}_2}{\partial \mathrm{U}_1} & \frac{\partial \mathrm{R}_2}{\partial \mathrm{U}_2} & \cdots & \frac{\partial \mathrm{R}_2}{\partial \mathrm{U}_{\mathrm{N}}} \\ \vdots & \vdots & \ddots & \vdots \\ \frac{\partial \mathrm{R}_{\mathrm{N}}}{\partial \mathrm{U}_1} & \frac{\partial \mathrm{R}_{\mathrm{N}}}{\partial \mathrm{U}_2} & \cdots & \frac{\partial \mathrm{R}_{\mathrm{N}}}{\partial \mathrm{U}_{\mathrm{N}}} \end{bmatrix}. \tag{12}$$

Each term $\mathbf{P}_{i,j}$ consists of five components and they result from the inviscid numerical flux Jacobian, $\mathbf{C}_{\mathrm{i}}$, the viscous flux Jacobian, $\mathbf{C}_{\mathrm{v}}$, and the source Jacobians due to axisymmetric coordinate system, $\mathbf{C}_{\mathrm{a}}$, the source Jacobian due to turbulence, $\mathbf{C}_{\mathrm{t}}$, and the source Jacobian due to chemistry, $\mathbf{C}_{\mathrm{c}}$. The evaluation of each of these Jacobian matrices is discussed below.

The inviscid numerical flux Jacobian at each cell face is evaluated by the solutions of a Riemann problem in a rotated frame aligned with the normal to the cell face and takes on the form of

$$\mathbf{C}_i = \frac{\partial(\vec{\mathbf{F}} \cdot \vec{n})}{\partial \mathbf{U}_{i,j}} = \frac{\partial \mathbf{F}}{\partial \mathbf{F}^*}\frac{\partial \mathbf{F}^*}{\partial \mathbf{U}^*_{\mathrm{L/R}}}\frac{\partial \mathbf{U}^*_{\mathrm{L/R}}}{\partial \mathbf{U}_{i,j}}, \tag{13}$$

where $\mathbf{U}^*_{\mathrm{L/R}}$ and $\mathbf{F}^*$ are the solution state and flux in the rotated frame. The term $\frac{\partial \mathbf{F}^*}{\partial \mathbf{U}^*_{\mathrm{L/R}}}$ is evaluated for both the Roe and HLLE flux functions. This inviscid Jacobian evaluation is approximated by assuming that the eigenvalues and eigenvectors (appearing in Roe and HLLE flux functions) are constant and, when using higher order scheme, the gradients of the primitive variables are also assumed to be constant. Pierce and Giles (1997) also suggested that using the matrix precondition based on a first-order discretization for higher-order schemes is acceptable.

The viscous numerical flux Jacobian is formulated depending on the method used to evaluate the viscous flux. In this study, the viscous numerical flux Jacobian is determined using a diamond-path procedure. The general form for the viscous flux Jacobian is

$$\mathbf{C}_{\mathrm{v}} = \frac{\partial \vec{\mathbf{F}}_{\mathrm{v}} \cdot \vec{n}}{\partial \mathbf{U}_{i,j}} = \frac{\partial \Big(n_{\mathrm{r}}\ \mathbf{F}_{\mathrm{v}} + n_{\mathrm{z}}\ \mathbf{G}_{\mathrm{v}} \Big)}{\partial \mathbf{U}_{i,j}}\,. \tag{14}$$

In the source Jacobians, $\mathbf{C}_{\mathrm{s}}$, the three terms are lumped together as

$$\mathbf{C}_{\mathrm{s}} = -\frac{\partial(\frac{\mathbf{S}_{\mathrm{a}\mathbf{i,j}}}{r})}{\partial \mathbf{U}_{i,j}} + \frac{\partial \mathbf{S}_{\mathrm{t}i,j}}{\partial \mathbf{U}_{i,j}} + \frac{\partial \mathbf{S}_{\mathrm{c}i,j}}{\partial \mathbf{U}_{i,j}}\,. \tag{15}$$

The preconditioner was tested using a finite-difference method with a first order accurate approximation of the residual Jacobian:

$$\left.\frac{\partial \mathbf{R}_{i,j}(\mathbf{U}, \nabla \mathbf{U})}{\partial \mathbf{U}}\right|_{i,j} \approx \frac{\mathbf{R}(\mathbf{U}_{i,j} + \epsilon) - \mathbf{R}(\mathbf{U}_{i,j})}{\epsilon} + \mathcal{O}(\epsilon)\,,$$

where $\epsilon = \eta \mathbf{U}$ with $\eta = 10^{-6} \sim 10^{-5}$. The verification has been performed with varied solution fields and different mesh stretching factors. The observed maximum relative error was found to be about

$$\sigma = \left| \frac{\frac{\partial \mathbf{R}}{\partial \mathbf{U}_{i,j}} - \frac{\mathbf{R}(\mathbf{U}_{i,j}+\epsilon) - \mathbf{R}(\mathbf{U}_{i,j})}{\epsilon}}{\frac{\partial \mathbf{R}}{\partial \mathbf{U}_{i,j}}} \right| \leq 2.0\%\,. \tag{16}$$

It is felt that this error is acceptable considering the approximations used in the Jacobian evaluation and the numerical error associated with the numerical scheme.

3.3.2 Restriction and Prolongation Operators

In particular, it was found that the multigrid convergence was significantly affected by the prolongation operator. A standard bi-linear interpolation was used initially to transfer corrections from coarse to fine mesh; however, the performance of the multigrid scheme suffered. Convergence was hampered and, in some cases, the procedure failed to converge. In this work, efforts have been made to devise more effective prolongation operators for meshes with large cell aspect ratios.

Figure 1 illustrates a stretched grid. Several prolongation operators are investigated: simple injection, $\mathbf{U}_{i,j\ \mathrm{fine}} = \mathbf{U}_{i,j\ \mathrm{coarse}}$; area weighted injection, $\mathbf{U}_{\mathbf{i,j}\ \mathrm{fine}} = (A_{i,j\ \mathrm{coarse}}/\sum A_{i,j\ \mathrm{fine}})\ \mathbf{U}_{i,j\ \mathrm{coarse}}$; a standard bi-linear interpolation; and finally, a standard bi-linear interpolation plus a linear interpolation, meaning that interpolating the value for the coarse node (i,j) using standard bi-linear first and then interpolating for the fine cell (i,j) with values from both coarse node (i,j) and coarse cell (i,j) with a linear interpolation. The effectiveness of using these different prolongation operators has been studied for a laminar non-reacting flow problem using stretched computational grids. Based on this study, it is suggested that a cell-aspect-ratio-based sensor can be applied as a switch in the approach of the prolongation operator. A cell-aspect-ratio-based sensor was implemented in the multigrid algorithm as follows: simple injection is used for cells with aspect ratio higher than a cutoff value, and standard bi-linear interpolation is then employed for cells with aspect ratios lower than that cutoff value.

Note that the multigrid algorithm is applied directly to each of the solution blocks without regard to the level of refinement for the grid blocks associated with each solution block, i.e., the grids are not necessarily on the same refinement level due to the AMR procedure. This block-based approach to the multigrid algorithm can adversely affect its performance. This performance degradation may be remedied by utilising additional multigrid levels spanning across blocks to bring all solution content to the same level of refinement, but this is not considered here. In addition, the system of governing equations is solved on the coarsest grid level. The communication for the multigrid is then carried out on the coarsest grids between blocks. The number of inter-block messages on the coarsest meshes is often nearly the same as that on the fine meshes, thereby the ratio of computation to communication may decrease and the parallel performance would be adversely affected.

3.4 Block-Based Adaptive Mesh Refinement

A flexible block-based hierarchical data structure has been developed and is used in conjunction with the finite-volume scheme described above to facilitate automatic solution-directed mesh adaptation on multi-block body-fitted quadrilateral mesh according to physics-based refinement criteria. In a block-based AMR strategy, mesh adaptation is accomplished by the dividing and coarsening of appropriate solution blocks. In general, each block also has an equal number of cells. The basic data structure is then a tree, where any block that requires refinement generates a number of equal sized blocks when a resolution change of two is assumed. The block-based AMR strategy results in a rather light tree data structure for prescribing the connectivity between blocks as compared to the tree structure generally used for tracking cell connectivity in the cell-based methods. In addition, the block-based data structure naturally lends itself towards an efficient and readily scalable parallel implementation. It amortizes the overhead of communication over entire blocks of cells, instead of over single cells as in cell-based data structures. However, generally larger numbers of refined cells can be created (i.e., typically more than the corresponding number of cells used in cell-based tree data structures) thereby possibly increasing the amount of computational work and storage space needed to solve a given problem.

Applications of the block-based approach on Cartesian mesh are described, for example, by Quirk and Hanebutte (1993), Berger and Saltzman (1994), Gombosi and co-workers (1994), and MacNeice et. al. (2000). Following Groth et al. (1999, 2000) for computational magnetohydrodynamics, a flexible block-based hierarchical data structure to facilitate automatic solution-directed mesh adaptation on multiblock body-fitted (curvilinear) meshes for complex flow geometries has been developed. While introducing some added complications, the use of body-fitted meshes permits more accurate solutions near boundaries, enables the use of anisotropic grids with grid point clustering and stretching, and allows for better resolution of thin boundary and mixing layers. Note that, in this study, the mesh refinement is constrained such that the grid resolution changes by only a factor of two between adjacent blocks and the minimum resolution is not less than that of the initial mesh. Standard multigrid-type restriction and prolongation operators are used to evaluate the solution on all blocks created by the coarsening and division processes, respectively.

We use a heuristic set of refinement criteria based on our physical understanding of the flow properties of interest (so-called physics-based refinement criteria). For the non-reacting flows considered here, the following measures are used $\epsilon_1 \propto |\vec{\nabla}\rho|\,, \epsilon_2 \propto |\vec{\nabla}\cdot\vec{u}|\,, \epsilon_3 \propto |\vec{\nabla}\otimes\vec{u}|$, in the decision to refine or coarsen a solution block. These three quantities correspond to local measures of the density gradient, compressibility, and vorticity of the mean flow field and enable the detection of contact surfaces, shocks, and shear layers. For combusting flows, additional measures were identified for directing the mesh adaption. The following four additional measures, $\epsilon_4 \propto |\vec{\nabla}k|\,, \epsilon_5 \propto |\vec{\nabla}\omega|\,, \epsilon_6 \propto |\vec{\nabla}T|\,, \epsilon_7 \propto |\vec{\nabla}c_{\mathrm{n}}|$ are used. The first two measures correspond to gradients of the specific turbulent kinetic energy and dissipation rate per unit turbulent kinetic energy, respectively, and relate to the structure of the turbulent field. The last two quantities measure the gradients of mean temperature and mean concentration for species n, respectively, and provide reliable detection of flame fronts and combustion zones for reactive flows.

3.5 Domain Decomposition and Parallel Implementation

Domain decomposition is carried out by farming the solution blocks out to the separate processors, with more than one block permitted on each processor. For homogeneous architectures, an effective load balancing is achieved by simply distributing the blocks equally among the processors. For heterogeneous parallel machines, a weighted distribution of the blocks can be adopted to preferentially place more blocks on the faster processors and less blocks on the slower processors.

Placing nearest-neighbour blocks on the same processor can also help to reduce the overall communication costs. A Morton ordering space-filling curve (Aftosmis et al. (2004)) is adopted to provide nearest-neighbour ordering of the solution blocks in the multi-block quadrilateral AMR meshes (Figure 2), and improve the parallel performance of the solution method.

The parallel implementation of the block-based AMR scheme was developed using the C^{++} programming language (Stroustrup (2001)) and MPI (message passing interface) (Gropp et al. (1999)). Use of these standards greatly enhances the portability of the computer code. Inter-processor communication is mainly associated with block interfaces and involves the exchange of ghost-cell solution values and conservative flux corrections at every stage of the multi-stage time-integration procedure. Message passing of the ghost-cell values and flux corrections is performed in an asynchronous fashion with gathered wait states and message consolidation.

4 NUMERICAL VERIFICATION

The parallel implementation has been carried out on a parallel cluster of 4-way Hewlett-Packard ES40, ES45, and Integrity rx4640 servers with a total of 244 Alpha and Itanium 2 processors. A low-latency Myrinet network and switch is used to interconnect the servers in the cluster. All of the numerical results reported here were obtained using this parallel cluster. Initial verification of the proposed parallel AMR scheme is carried out by considering the numerical predictions for three classical non-reacting flow problems (a laminar Couette flow, a laminar flat plate boundary layer flow and a fully-developed turbulent pipe flow) and one reactive flow problem (a premixed laminar flame). The solutions for these problems are well established and can be used to assess the validity and accuracy of the scheme. Herein, we only present a laminar Couette flow, a fully-developed turbulent pipe flow and a premixed laminar flame to keep this section brief,

4.1 Laminar Couette Flow

The computation of non-reacting laminar Couette flow in a channel with a moving wall was considered in order to demonstrate the accuracy of the viscous spatial discretisation scheme. The case with an upper wall velocity of 29.4 m/s and a favourable pressure gradient of $dp/dx = -3,177$ Pa/m was investigated and compared to the analytic solution. The predicted velocity profile (not shown here) matches the exact analytic solution for this incompressible isothermal flow. The L_1-norm of the error in axial component of velocity is shown in Figure 3 for both the uniform and adaptive grids. The slope of the norm is 2.02, indicating that the finite-volume scheme is indeed second-order accurate.

4.2 Fully-Developed Turbulent Pipe Flow

A verification of the parallel AMR scheme for non-reacting turbulent flows has been performed. The numerical results of a non-reacting fully-developed turbulent pipe flow with $\mathrm{Re} = 500,000$ are compared to the experimental data of Laufer (1954). Solutions for both the wall function and low-Reynolds-number formulations of the k-ω turbulence model are compared to experimental mean axial velocity and turbulent kinetic energy profiles in Figures 4 and 5. Calculations with the low-Reynolds-number formulation were performed using 80 cells in the radial direction with 3-4 of those cells lying within the laminar sub-layer. The first cell off the wall was located at $y^+ \approx 0.6$. The results using the wall functions were obtained using 32 cells in the radial direction with the first cell located at $y^+ \approx 43$. The agreement between the experimental data and numerical results for this case is generally quite good. As expected, it is evident that the k-ω model is able to reproduce the characteristic features of fully-developed pipe flow.

4.3 Multigrid Acceleration

Convergence acceleration provided by the preconditioned multigrid algorithm was also examined for the fully developed turbulent pipe flow problem. A mesh of size 1,024 cells and having cell aspect ratios in the range of 10 to 2×10^5 and an off-wall spacing of 7.0×10^{-7} m was used in this study. There were 32 cells in the radial direction and an automatic wall boundary treatment was employed. The influence of using different multigrid levels and cycles on convergence features has also been investigated.

Figures 6 and 7 compare the convergence rates achieved for the turbulent pipe flow using the explicit time-marching scheme with local time-stepping, the multigrid algorithm with explicit smoother, and the preconditioned multigrid approach. The convergence rate is shown as a function of both the number of iterations and the number of equivalent right-hand side (RHS) evaluations. Clearly, the preconditioned multigrid results in a more efficient convergence rate than the others. Notice from the figures that the preconditioned multigrid algorithm exhibited a convergence stall after the residual in the turbulent kinetic energy dropped to about 10^4. It is believed that this effect is due to the non-linear nature of the slope limiters and their activation in smooth regions of the flow field (venkatakrishnan (1993)). This convergence stall can be alleviated by freezing the limiter after the residual has dropped to a predefined level; however, this technique was not employed here.

Tables 1–3 summarise some convergence features for the fully developed turbulent pipe flow problem. Note that the maximum grid level for these cases was chosen to be 3, allowing for relatively smaller-sized solution blocks. Table 1 lists the numerical data from using both the regular and the preconditioned multigrid and the results for grid-level and multigrid-cycle effects are presented in Table 2 and Table 3. The term work unit (WU) is defined as the time for one right-hand-side evaluation on the finest mesh.

Table 1 indicates that the preconditioned multigrid with 5-stage optimal smoothing scheme produces a 14 times speedup over multigrid without a preconditioner and is shown in Figure 8. For both cases, the L_2 norms of the residual for turbulent kinetic energy drop about six orders of magnitude. The data from Table 2 shows a speedup factor of four between the 3-level multigrid and the single-level computation. This grid-level influence on the convergence is shown in Figure 9. The convergence rate of 2-level is the same as that of a 3-level for this case, and both used the V-cycle. The same convergence rates for both 2- and 3-level might be due to the fact that the turbulence source terms were not recalculated on the coarse meshes. Figure 10 shows that the 3-level V- and W-cycle preconditioned multigrid algorithms, using a 5-stage optimal smoothing scheme, have nearly the same speedup in terms of multigrid cycles, while Table 3 indicates the V-cycle uses about half the computation time of the W-cycle. The reason might be that the W-cycle is expensive in a parallel algorithm when frequent coarse-level calculations lead to poor processor utilisation. From these results, it appears that a 3-level V-cycle preconditioned multigrid should deliver an optimal speed up for computing turbulent flows. For this reason, the 3-level V-cycle preconditioned multigrid was employed in the numerical predictions of the turbulent reactive and non-reactive flows that follow.

4.4 Premixed Laminar Flame

Verification of the proposed parallel AMR scheme for reactive flows is carried out by considering the numerical predictions of planar one-dimensional premixed methane-air laminar flames for a range of equivalence ratios and comparing the predictions to those obtained using the CHEMKIN program PREMIX. The six-species, two-step, reduced kinetic scheme for the oxidation of methane described above is used. CHEMKIN is a commercial software tool available from Reaction Design for solving complex chemical kinetics problems and PREMIX is a utility that can be used for predicting one-dimensional premixed flames. A detailed 17-species, 58-reaction kinetic scheme is used in the PREMIX calculations to represent the oxidation of methane. These comparisons provide a check of the algorithms ability to predict two key features of laminar flames: the flame temperature and laminar flame speed.

For the premixed flame predictions, a fixed (non-adapted) one-dimensional mesh with 400 non-uniformly space computational cells is used. The steady state or time-invariant structure of the flame is then obtained by starting with uniform fresh and burnt gas solution states at atmospheric and the adiabatic flame temperatures, respectively, and iterating until a steady-state solution is achieved with a stationary flame structure. The upstream and downstream boundary velocity and pressure are adjusted such that the mass flux is constant throughout the domain.

The numerical results for the premixed laminar flame are summarised in Figures 11 and 12 and Table 4. The table gives predictions of both the equilibrium temperature of the products, T, and the laminar flame velocity, s_L, as a function of the equivalence ratio ($\phi = 0.6$, 0.8, 1.0, and 1.2). These figures depict the predicted flame structure for $\phi = 1$ and show variation of the velocity, temperature, and mass fraction through the flame. The predicted laminar flame speed is $s_L = 40.6$ cm/s in this case and the temperature of the products (flame temperature) is $T = 2256$. The overall agreement between the two sets of results is very good, especially considering that the six-species two-step chemical kinetics scheme used by the parallel solver is greatly simplified in comparison to the 17-species, 58-reaction scheme used in the CHEMKIN calculations. This provides strong support for the validity of the proposed reactive flow solver.

It should be noted that the flow Mach numbers for the premixed laminar flames are very small ($M \approx 0.001 - 0.003$) and the low-Mach-number preconditioning is absolutely necessary for these cases in order to get accurate predictions of the flame structure with the proposed compressible finite-volume formulation.

5 RESULTS AND DISCUSSIONS

The parallel AMR method is applied to solutions of axisymmetric co-flow methane-air laminar and turbulent diffusion flames. The six-species, two-step, reduced kinetic scheme for the oxidation of methane is again used for the laminar diffusion flame calculations and the five-species, one-step, reduced kinetic scheme for the oxidation of methane is used for turbulent diffusion flame calculations.

5.1 Non-Premixed Laminar Diffusion Flame

The computational domain is rectangular in shape with dimensions of 10 cm by 5 cm. The axis of symmetry is aligned with the left boundary of the domain and the right far-field boundary is taken to be a free-slip boundary along which inviscid reflection boundary data is specified. The top or outlet of the flow domain is open to a stagnant reservoir at atmospheric pressure and temperature and Neumann-type boundary conditions are applied to all properties except pressure which is held constant. The bottom or inlet is subdivided into four regions (a innermost region of the fuel inlet, a small gap associated with the annular wall separating the fuel and oxidiser, a region of co-flowing oxidiser, and a far-field boundary along which free-slip boundary conditions are applied). Additional details concerning the setup for this diffusion flame can be found in the papers by Mohammed et al. (1998) and Day and Bell (2000). The solution domain is initialised with a uniform solution state corresponding to quiescent air at 298K, except for a thin region across the fuel and oxidiser inlets, which is taken to be air at 1500 K so as to ignite the flame. Note that the Mach and Reynolds number based on the fixed diluted methane flow in the fuel inlet are $M = 0.0016$ and $Re = 169$.

Figure 13 shows the computed isotherms and flame structure obtained using a sequence of adaptively refined grids starting from the initial mesh (96 solution blocks with 3,072 cells) and proceeding to the final mesh after five levels of refinement (396 blocks with 12,672 cells). The sequence of adaptively refined grids, showing both the solution blocks and computational cells, is also shown in Figure 14. The effect of the finer resolution can be clearly seen, as the flame structure becomes much sharpened and more resolved. Finally, Figure 15 shows the mass fractions of the combustion products.

A comparison of the results of Figures 13–15 with those given in the previous studies by Mohammed et al. (1998) and Day and Bell (2000) reveals, that in spite of the inherent simplifications used in the two-step reaction mechanism, the predicted flame structure agrees very well with the previous work. The "wishbone" structure of the high-temperature region is present and the computed lift-off and flame heights are 0.05 cm and 3.3 cm, respectively, with a maximum centre-line temperature of 2080 K. All of these values agree reasonably well with the previously published results. The predicted value of the carbon monoxide, CO, mass fraction concentration at $z = 3$ cm along the centre-line is $c_{\text{CO}} = 0.026$ and, considering the limitations of the reduced chemistry mechanism being used, is in reasonable agreement with those of Mohammed et al. (1998), who report a mass fraction of $c_{\text{CO}} = 0.03$ at the same location.

5.2 Non-Premixed Turbulent Diffusion Flame

The International Workshops on Measurement and Computation of Turbulent Non-Premixed Flames (TNF) has established an Internet library of well-documented experimental database for turbulent non-premixed flames that are appropriate for combustion model verification and validation. The Sydney bluff-body burner configuration shown in Figure 16 that forms part of this experimental database has data available for both non-reacting and reacting cases. The bluff-body has a diameter of $D_b = 50$ mm and is located in a co-axial flow of air. Various gases can be injected through an orifice of diameter 3.6 mm at the base of the cylindrical bluff body. The bluff-body stabilised flames have a recirculation zone close to the base of the bluff body. This burner configuration produces a relatively extensive and complex turbulent field and causes intense mixing between the reactants and combustion products. The stabilisation mechanisms resemble those of industrial combustors and yet the boundary conditions for the bluff-body flames are simple and well-defined, making them well suited for investigating in great detail the capabilities of models for turbulent non-premixed diffusion flames.

5.2.1 Bluff-Body Burner Non-reacting Flows

In the cold non-reacting bluff-body burner flow case, air is injected through the orifice at the base of the cylindrical bluff body with a temperature of 300 K and a bulk velocity of 61 m/s. The bulk velocity and temperature of the co-flowing air are 20 m/s and 300 K, respectively. The Reynolds and Mach numbers based on the high-speed jet are $\mathrm{Re}=193,000$ and $\mathrm{Ma}=0.18$.

We have examined predicted solutions on a sequence of refined meshes to establish the grid-convergence of the solution. The flow field predictions have been computed on a sequence of adaptively refined grids, 5 16×16 cell blocks and 1,280 cells, 14 16×16 cell blocks and 3,584 cells, 26 16×16 cell blocks and 6,656 cells, and 53 16×16 cell blocks and 13,568 cells. The mesh resolution was such that the typical size of the computational cells nearest the wall was in the range $0.2 < y^+ < 1$. It is apparent that the majority of the solution parameters do not change as the mesh is refined from 6,656 cells to 13,568 cells, as shown in Figures 20–23. The numerical solutions can be said to be virtually grid independent.

Figure 17 shows the predicted mean velocity and streamlines and reveal the formation of a double-vortex structure in the re-circulation zone which are important in controlling fuel/oxidiser mixing. The calculations indicate that the re-circulation zone extends to $x/D_b \approx 0.8$. This is slightly less than the experimentally observed value of $x/D_b \approx 1.0$. The agreement between the predictions and experiment is further confirmed by a comparison of the predicted radial profiles of the mean axial velocity component at $x/D_b=0.6$ and $x/D_b=1.0$ downstream from the base of the bluff-body to the measured data as shown in Figure 18 and 19, and by a comparison of the predicted axial (centreline) profile of the mean axial velocity component to experimental results as depicted in Figure 20. The predicted root mean square (RMS) fluctuations of the velocity components and specific Reynolds stress ($\overline{u'v'}$) are also compared to the experimental data in Figures 21, 22 and 23. It can be seen that there are under- and/or over-predicted regions ($r/R_\mathrm{b} < 0.2$). These regions encompass the inner vortex and the vicinity of the outer vortex of a double-vortex structure in the re-circulation zone. Re-circulation zones with complex turbulent structures are quite sensitive to the turbulence modelling and a variety of RANS simulations have addressed this sensitivity to the turbulence model and/or combustion models (Dally et al. (1998); Xu (2000); Merci (2001); Liu et al. (2005)). The overall agreement between the numerical solution and the experimental data for these turbulence quantities is quite reasonable and is comparable to other results reported in the literature (Dally et al. (1998); Turpin and Troyes (2000); Merci (2001)).

For the ethylene jet case, ethylene (C_2H_4) is injected at the base of the bluff-body with a velocity of 50 m/s and a temperature of 300 K. In this case, the Reynolds and Mach numbers based on the ethylene flow are $\mathrm{Re}=145,000$ and $\mathrm{Ma} = 0.11$. Numerical results for the ethylene fuel jet are depicted in Figure 24, where the predicted mass fraction of C_2H_4 obtained using a mesh consisting of 479 6×6 cell blocks and 17,244 cells, with five levels of refinement, is compared to measured C_2H_4 concentrations. The mesh resolution was also such that the typical size of the computational cells nearest the wall was in the range $0.2 < y^+ < 1$. The predictions of the mixing field (Figure 24) also appear to be quite reasonable when compared to the experimental data. Detailed comparisons of the predicted on-axis axial and radial distributions at $x/D_b=1.0$ of the mean C_2H_4 mass fraction to measured values given in Figures 25–26 also indicate that the fuel and oxidiser mixing process is quite well reproduced.

5.2.2 Bluff-Body Burner Reacting Flow

For the reacting case, methane (CH_4) is injected through the orifice at the base of the cylindrical bluff body with a temperature of 300 K. The bulk velocities of the co-flowing air and methane fuel are 25 m/s and 108 m/s, respectively. The Reynolds and Mach numbers of the methane jet are $\mathrm{Re}=315,000$ and $\mathrm{Ma}=0.24$.

Computations were carried out on a sequence of adaptively refined grids, 7 16×16 cell blocks and 1,792 cells, 28 16×16 cell blocks and 7,168 cells, 70 16×16 cell blocks and 17,920 cells, 97 16×16 cell blocks and 24,832 cells, and 112 16×16 cell blocks and 31,744 cells to assess the grid independence of the predictions. As in the non-reacting cases, the mesh resolution was such that the typical size of the computational cells nearest the wall was in the range $0.2 < y^+ < 1$. The results of the refinement study are shown in Figures 27-30, and the majority of the solution parameters, such as, axial velocity, temperature, and major species CO_2, do not change as the mesh is refined from 24,832 cells to 31,744 cells. The grid convergence solution is achieved.

Figure 31 shows the predicted distributions of mean temperature and mean mass fraction of CO_2 for this turbulent non-premixed flame. The predicted flame structure is generally in agreement with the experimentally observed structure. The flame is quite elongated and three zones can be identified: the re-circulation, neck, and jet-like propagation zones. A vortex structure is formed in the re-circulation zone and acts to stabilise the flame. The maximum flame temperature is about 2180 K. The predicted mean temperature, 1350 K, and mass fraction of CO_2, 0.1, at location of ($x/D_b = 1.92$, $r/R_b = 0.4$) are compared to the measured values of the flame temperature, 1120 K, and carbon dioxide concentration, 0.07. The temperature and hence carbon dioxide concentration are somewhat over-predicted. However, the agreement with the experimental values is reasonable considering the limitations of the simplified reduced chemical kinetics scheme and turbulence/chemistry interaction model used herein, as well as the fact that radiation transport is not taken into account in the simulation.

5.3 Multigrid Acceleration

The numerical solutions for both the cold and hot cases of the two-dimensional axisymmetric bluff-body burner flows were obtained using the preconditioned multigrid technique. The 3-level V-cycle preconditioned multigrid with a 3-stage optimally smoothing scheme was employed. A prolongation operator, based on a cell-aspect-ratio sensor as discussed above, was also applied. For those cells with aspect ratios greater than a value of 1000, a simple injection was used. Standard bi-linear interpolation was employed for cells with aspect ratios smaller than this value. The CFL number was 0.2.

Both the multigrid and preconditioned multigrid algorithms speed up the convergence rates to the steady-state solutions quite significantly for both cases as compared to the convergence rate achieved using the semi-implicit time-marching method alone (i.e., smoother alone without the multigrid procedure). The preconditioned multigrid seems to have a more positive effect for the reacting case than for the non-reacting problem. Although the convergence rate slows after the residual has been reduced by 4–5 orders of magnitude, and this slow down may be associated with limitations of the proposed multigrid method when AMR is used, overall it is felt that satisfactory convergence rates have been achieved. The preconditioned multigrid provides a speedup of about two in terms of CPU time over regular multigrid for both cases.

5.4 Parallel Performance

Parallel speedup (strong scaling), parallel scale-up (weak scaling), and parallel efficiency are often used to measure/evaluate the parallel performance of a parallel algorithm. The parallel speedup, S_p, is defined as $S_p = t_1/t_p$, the parallel scale-up, S_ϕ, defined as $S_\phi = t_1/t_p\ p$, and the parallel efficiency, E_p is defined as $E_p = S_p/p$, where t_1 is the time required to solve the problem by a single processor, and t_p is the time required to solve the problem by p processors. While both the parallel speedup and the parallel scale-up are important to consider, the parallel speedup is probably more relevant for engineering problems of practical interest. High efficiency for strong scaling is generally harder to achieve than for the weak scaling problem. Herein, the parallel speedup and efficiency of the proposed parallel solution-adaptive algorithm applied to three flow problems (a laminar diffusion flame, a turbulent pipe flow, and a turbulent diffusion flame) have been assessed.

For the laminar diffusion flame problem, Figure 32 shows that the parallel speed-up of the block-based AMR scheme is linear and is 90% efficient for up to 32 processors using the larger (10×10) solution blocks. For the smaller (8×8) blocks, the efficiency drops slightly down to 80% efficient. Figure 33 shows that the parallel speedup of the block-based AMR scheme for the turbulent pipe flow problem is nearly linear and is at least 90% efficient for up to 32 processors using the larger (10×10) solution blocks. For the smaller (8×8) blocks, the efficiency drops slightly down to 87% efficient. The rather high level of performance should generally be expected for the two-dimensional algorithm with the explicit time marching scheme.

The parallel performance of the proposed algorithm is further assessed for a fixed-size turbulent diffusion flame problem using up to 64 processors. An added difference of this parallel performance assessment from the previous ones is the use of 3-level V-cycle preconditioned multigrid technique in the computations. It can be observed in Figure 34 that the proposed scheme provides a nearly linear speedup and is about 76% efficient for up to 64 processors using the larger 24×24 cell solution blocks. For the smaller 16×16 cell solution blocks, the parallel efficiency drops to 68%. Compared to the estimation shown in Figure 33, the parallel efficiency is somewhat reduced. The performance is affected by the coarse grid calculations of the multigrid algorithm. As mentioned earlier, the number of inter-block messages on the coarse meshes is often nearly the same as that on the fine meshes, thereby decreasing the ratio of computation to communication and adversely affecting the parallel performance.

6 CONCLUSIONS

A highly scalable parallel AMR scheme has been described for non-premixed combusting flows. The combination of a block-based AMR strategy and parallel implementation has resulted in a powerful computational tool, as demonstrated by the numerical results for both laminar and turbulent non-premixed flames. The predicted flame structure of an axisymmetric co-flow methane-air laminar diffusion flame, including the computed lift-off, flame heights and the maximum centre-line temperature, agrees reasonably well with the previously published results. A quantitative evaluation of the parallel AMR algorithm has also been carried out for a complex turbulent combusting flow in a bluff-body burner having a relatively complex physical geometry. For complex turbulent combusting flows, dealing with the near-wall turbulence is challenging within an AMR procedure. This study proposed a somewhat novel automatic and smooth switching procedure for computing wall turbulence that is well suited to the AMR scheme considered here. In order to provide enhanced convergence for steady-state problems, a preconditioned (matrix preconditioner) multigrid strategy has been proposed and developed for two-dimensional turbulent combustion calculations. It is thought to be one of the first applications of a parallel AMR scheme with multigrid to turbulent-combusting flow calculations in the literature, and significantly improved convergence was achieved by devising a cell-aspect-ratio-based prolongation operator for treating highly stretched meshes. This numerical study demonstrates the validity and potential of the parallel AMR approach for predicting fine-scale features of complex turbulent non-premixed flames.

7 ACKNOWLEDGEMENT

The first author is very grateful to Prof. Clinton P. T. Groth and University of Toronto for the financial support provided throughout this research.

REFERENCES

Aftosmis, M. J., Berger, M. J. and Melton, J. E. (1998) ‘Robust and Efficient Cartesian Mesh Generation for Component-Base Geometry’, *AIAA Journal*, Vol. 36, pp. 952–960.

Aftosmis, M. J., Berger, M. J., and Murman, S. M. (2004) ‘Applications of Space-Filling Curves to Cartesian Methods for CFD’, AIAA Paper, 2004, 2004-1232.

Barth, T. J. (1993) ‘Recent Developments in High Order K-Exact Reconstruction on Unstructured Meshes’, AIAA Paper, 1993, 93-0668.

Bell, J. B., Day, M. S., Almgren, A. S., Lijewski, M. J. and Rendleman, C.A. (2001) ‘Adaptive Numerical Simulation of Turbulent Premixed Combustion’, *Proceedings of the First MIT Conference on Computational Fluid and Solid Mechanics*, June 2001.

Bell, J. B., Day, M. S., Almgren, A. S., Lijewski M. J. and Rendleman, C. A. (2002) ‘A Parallel Adaptive Projection Method for Low Mach Number Flows’, *International Journal for Numerical Methods in Fluids*, Vol. 40, pp. 209-216.

Bell, J. B. and Day, M. S. and Grcar, J. F. (2002) ’Numerical Simulation of Premixed Turbulent Methane Combustion’, *Proceedings of the Combustion Institute*, Vol. 29, 2002, pp.1987-1993.

Berger, M. J. (1984) ‘Adaptive Mesh Refinement for Hyperbolic Partial Differential Equations’, *Journal of Computational Physics*, Vol. 53, pp. 484–512.

Berger, M. J. and Colella, P. (1989) ‘Local Adaptive Mesh Refinement for Shock Hydrodynamics’, *Journal of Computational Physics*, Vol. 82, pp. 67–84.

Berger, M. J. and Saltzman, J. S. (1994) ‘AMR on the CM-2’, *Applied Numerical Mathematics*, Vol. 14, pp. 239–253.

Bussing, T. R. A. and Murman, E. M. (1987) ‘Numerical investigation of two-dimensional H_2-air flameholding over ramps and rearward-facing steps’, *J. Propulsion*,Vol. 3, pp.448-454.

Bussing, T. R. A. and Murman, E. M. (1988) ‘Finite-volume method for the calculation of compressible chemically reacting flows’, *AIAA Journal*,Vol. 26, pp.1070-1078.

Coirier, W. J. and Powell, K. G. (1996) ‘An Adaptively-Refined, Cartesian, Cell-Based Scheme for the Euler and Navier-Stokes Equations’,*AIAA Journal*, Vol. 34, No. 5, May 1996, pp. 938–945.

Dally, B. B., Fletcher, D. F. and Masri, A. R. (1998) ‘Flow and Mixing Fields of Turbulent Bluff-Body Jets and Flames’, *Combustion Theory and Modelling*, Vol. 2, 1998, pp. 193–219.

Day, M. S. and Bell, J. B (2000) ‘Numerical Simulation of Laminar Reacting Flows with Complex Chemistry’, *Combustion Theory and Modelling* , Vol. 4, No. 4, pp. 535–556.

De Zeeuw, D. and Powell K. G. (1993) ‘An Adaptively Refined Cartesian Mesh Solver for the Euler Equations’, *Journal of Computational Physics*, Vol. 104, pp. 56–68.

Einfeldt, B. (1988) ‘On Godunov-Type Methods for Gas Dynamics’, *SIAM Journal on Numerical Analysis*, Vol. 25, 1988, pp. 294–318.

Gao, X. (1997) ‘A Parallel Solution-Adaptive Method for Turbulent Non-Premixed Combusting Flows’, *Phd Thesis* ,University of Toronto, 2008.

Gerlinger, P. and Brüggemann, D. (1997) ‘Multigrid Convergence Acceleration for Turbulent Supersonic Flows’, *International Journal for Numerical Methods in Fluids*, Vol. 24, No. 10, 1997, pp. 1019–1035.

Gerlinger, P., Stoll, P. and Brüggemann, D. (1998) ‘An Implicit Multigrid Method for the Simulation of Chemically Reacting Flows’, *Journal of Computational Physics*, Vol. 146, 1998, pp. 322–345.

Gerlinger, P., Möbus, Helge and Brüggemann, D. (2001) ‘An Implicit Multigrid Method for Turbulent Combustion’, *Journal of Computational Physics*, Vol. 167, (2001), pp. 247–276.

Gombosi, T. I. and Powell K. G. and De Zeeuw, D. L. (1994) ‘Axisymmetric Modeling of Cometary Mass Loading on an Adaptively Refined Grid: MHD Results’, *Journal of Geophysical Research*, Vol. 99, 1994, pp.21525-21539.

Gordon, S. and McBride, B. J. (1994) ‘Computer Program for Calculation of Complex Chemical Equilibrium Compositions and Applications I. Analysis’, Reference Publication 1311, NASA, 1994.

Groth, C. P. T, De Zeeuw, D. L., Marshall, H. G., Gombosi,T. I., Powell, K. G. and Stout Q. F. (1999) ‘A Parallel Solution-Adaptive Scheme for Ideal Magnetohydrodynamics’, AIAA Paper, 1999, 99-3273, June 1999.

Groth, C. P. T, De Zeeuw, D. L., Gombosi, T. I., and Powell, K. G (2000) ‘Global Three-Dimensional MHD Simulation of a Space Weather Event: CME Formation, Interplanetary Propagation, and Interaction with the Magnetosphere’, *Journal of Geophysical Research* Vol. 105, No.A11, pp. 25,053–25,078.

Gropp, W., Lusk, E. and Skjellum, A. (1999) *Using MPI*, MIT Press, Cambridge, Massachussets, 1999.

Laufer, J. (1954) ‘The Structure of Turbulence in Fully Developed Pipe Flow’, Report 1174, NACA, 1954.

Linde, T. (2002) ‘A practical, general-purpose, two-state HLL Riemann solver for hyperbolic conservation laws’, *International Journal for Numerical Methods in Fluids*, Vol. 40, 2002, pp. 391–402.

Liu, K. and Pope, S. B. and Caughey, D. A. (2005) ‘Calculations of Bluff-Body Stabilized Flames Using a Joint Probability Density Function Model with Detailed Chemistry’, *Combustion and Flame* , Vol. 141, pp. 89–117.

McBride, B. J. and Gordon, S. (1996) ‘Computer Program for Calculation of Complex Chemical Equilibrium Compositions and Applications II. Users Manual and Program Description’, Reference Publication 1311, NASA, 1996.

MacNeice, P. and Olson, K. M. and Mobarry, C. and Fainchtein, de R. and Packer, C. (2000) ’PARAMESH: A parallel adaptive mesh refinement community toolkit’,*Computer Physics Communications* 2000, 126, pp.330–354.

Magnussen, B. F. and Hjertager B. H. (1976) ‘On Mathematcal Modeling of Turbulent Combustion with Special Emphasis on Soot Formation and Combustion’, 16th Symp. (Int.) on Combustion (1976). Comb. Inst., Pittsburg, Pennsylvania, pp. 719-729.

Mason, E. A. and Saxena S. C. (1958) ’An approximate formula for the thermal conductivity of multicomponent gas mixtures’, Phys. Fluids, 1958, 1, pp.361–369.

Mavriplis, D. J. (1998) ‘Multigrid Strategies for Viscous Flow Solvers on Anisotropic Unstructured Meshes’, *Journal ofComputational Physics*, Vol. 145, 1998, pp. 141–165.

Merci, B.(2001) and Dick, E. and Vierendeels, J. and Roekaerts D. and Peeters, T. W. J. ‘Application of a New Cubic Turbulence Model to Piloted and Bluff-Body Diffusion Flames’, *Combustion and Flame* , Vol. 126, pp. 1533–1556.

Mohammed, R. K., Tanoff, M. A., Smooke, M. D., Schaffer, A. M. and Long M. B., ‘Computational and Experimental Study of a Forced, Time-Varying, Axisymmetric, Laminar Diffusion Flame’, *Twenty-Seventh Symposium (International) on Combustion* , The Combustion Institute, Pittsburgh, 1998, pp. 693–702.

Pierce, N. A. and Giles, M. B. (1996) ’Preconditioning Compressible Flow Calculations on Stretched Meshes’, AIAA Paper 1996, 96-0889.

Pierce, N. A. and Giles, M. (1996) ’Preconditioned multigrid methods for compressible flow calculations on stretched meshes’, *Journal of Computational Physics*, Vol. 136, 1997, pp. 425–445.

Powell, K. G., Roe, P. L. and Quirk, J. J. (1993) ‘Adaptive-Mesh Algorithms for Computational Fluid Dynamics’, *Algorithmic Trends in Computational Fluid Dynmaics*, edited by Hussaini, M.Y., Kumar, A. and Salas, M.D., Springer-Verlag, New York, 1993, pp. 303–337.

Quirk, J. J. (1991) ‘An Adaptive Grid Algorithm for Computational Shock Hydrodynamics’, Ph.D. thesis, Cranfield Institute of Technology, January 1991.

Quirk, J. J. and Hanebutte, U. R. (1993) ‘A Parallel Adaptive Mesh Refinement Algorithm’, Report 93-63, ICASE, August 1993.

Roe, P. L. (1981) ‘Approximate Riemann Solvers, Parameter Vectors, and Difference Schemes’, *Journal of Computational Physics*, Vol. 43, 1981, pp. 357–372.

Schlichting, H.(1979) *Boundary-Layer Theory* , 7th Edition, McGraw-Hill, Toronto, 1979.

Sheffer, S. G., Martinelli, L. and Jameson, A. (1998) ‘An efficient multigrid algorithm for compressible reactive flows’, *J. Comput. Phys.* , Vol. 144, 1998, pp. 484–516.

Stroustrup, B.(1979) *The C++ Programming Language* , 4th Edition, Addison-Wesley, 2001.

Turkel, E. (1999) ‘Preconditioning Techniques in Computational Fluid Dynamics ’, *Annual Review of Fluid Mechanics*, Vol. 31, 1999, pp. 385–416.

Turpin, G. and Troyes, J. (2000) ‘Validation of a Two-Equation Turbulence Model for Axisymmetric Reacting and Non-Reacting Flows’, AIAA Paper, 2000, 2000-3463.

van Leer, B., Tai, C. H. and Powell, K. G. (1999) ‘Design of Optimally-Smoothing Multi-Stage Schemes for the Euler Equations’, AIAA Paper, 1989, 89-1933-CP.

Venkatakrishnan, V. (1993) ‘On the Accuracy of Limiters and Convergence to Steady State Solutions’, AIAA Paper, 1993, 93-0880.

Weiss, J. M. and Smith, W. A. (1995) ‘Preconditioning Applied to Variable and Constant Density Flows’, *AIAA Journal*, Vol. 33, No. 11, 1995, pp. 2050–2057.

Westbrook, C. K. and Dryer, F. L. (1981) ‘Simplified Reaction Mechanisms for the Oxidation of Hydrocarbon Fuels in Flames’, *Combustion Science and Technology*, Vol. 27, pp. 31–43.

Wilcox, D. C. (2002) *Turbulence Modeling for CFD*, DCW Industries, La Cañada, 2002.

Wilke, C. R. (1950) ‘A Viscosity Equation for Gas Mixtures’, *Journal of Chemical Physics*, Vol. 18, pp. 517–519.

Xu, J. and Pope, S. B. (2000) 'PDF Calculations of Turbulent Nonpremixed Flames with Local Extinction', *Combustion and Flame* , Vol. 123, pp. 281–307.

TNF, http://www.ca.sandia.gov/TNF/.

Smith, G. P., Golden, D. M., Frenklach, M., Moriarty, N. W., Eiteneer, B., Goldenberg M., Bowman, C. T., Hanson, R. K., Song, S., Gardiner, W. C., Lissianski, V. V. and Qin, Z., GRI-Mech 3.0, http://www.me.berkeley.edu/gri_mech/.

Table 1: Matrix-preconditioner effects on convergence of the 4-level V-cycle multigrid for the fully-developed turbulent pipe flow.

Method	CPU time [min]	WUs	Speedup
Multigrid	210.5	17542	1
Preconditioned multigrid	15	1250	14

Table 2: Grid-level effects on convergence of the V-cycle preconditioned multigrid for the fully-developed turbulent pipe flow.

Method	CPU time [min]	WUs	Speedup
Single-level	35.8	2983	1
2-level	10.9	908	3.3
3-level	9.69	807.5	3.7

Table 3: The V- and W-cycle effects on convergence of the 3-level preconditioned multigrid for the fully-developed turbulent pipe flow.

Method	CPU time [min]	WUs	Speedup
W-cycle	38	3166.7	1
V-cycle	22	1833.3	1.72

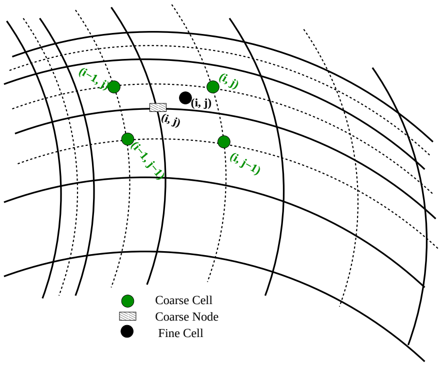

Figure 1: Illustration of different prolongation operators on a stretched body-fitted quadrilateral mesh.

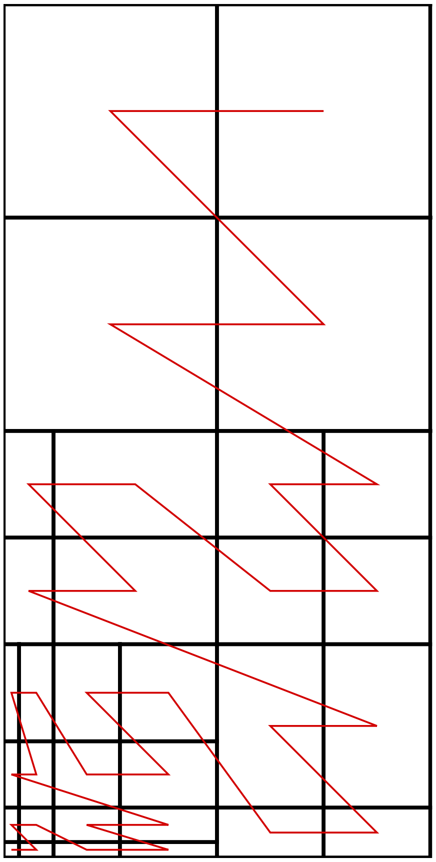

Figure 2: Morton ordering space filling curve used to provide nearest-neighbour ordering of blocks for more efficient load balancing of blocks on multiple processors. The thick black line represents the space filling curve passing through each of the solution blocks in the multi-block AMR mesh.

	Solution Method	Equivalence Ratio, ϕ			
		0.6	0.8	1.0	1.2
T (K)	PREMIX	1656	1993	2234	2143
	Current	1650	1995	2256	2221
s_L (cm/s)	PREMIX	12.15	29.1	41.0	38.6
	Current	13.3	29.4	40.6	38.5

Table 4: Comparison of the predictions of the parallel AMR algorithm using the two-step methane reduced mechanism to those of the CHEMKIN PREMIX program with detailed chemistry for various equivalence ratios. Predictions of both the equilibrium temperature of the products, T, and the laminar flame velocity, s_L, are shown for $\phi = 0.6$, 0.8, 1.0, and 1.2.

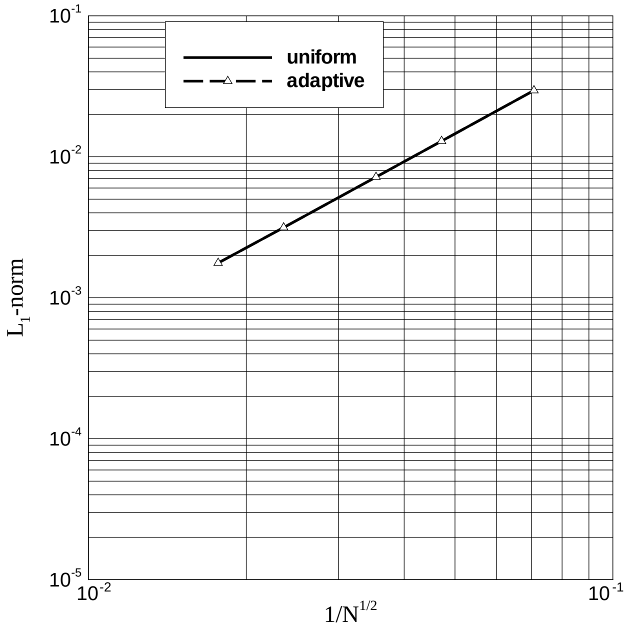

Figure 3: L_1-norms of the solution error as a function of mesh size for laminar Couette flow.

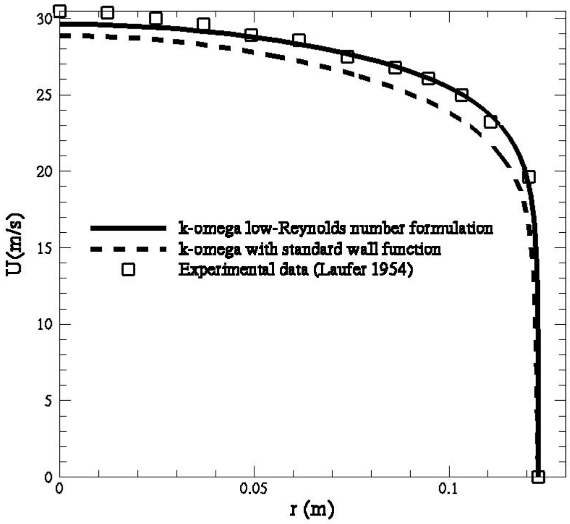

Figure 4: Comparison of predicted mean axial velocity with experimental data for fully developed pipe flow, Re$=500,000$.

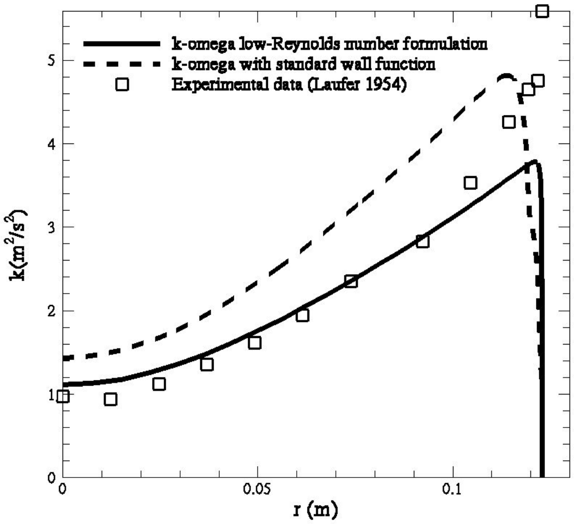

Figure 5: Comparison of predicted turbulent kinetic energy with experimental data for fully developed pipe flow, Re$=$ $500,000$.

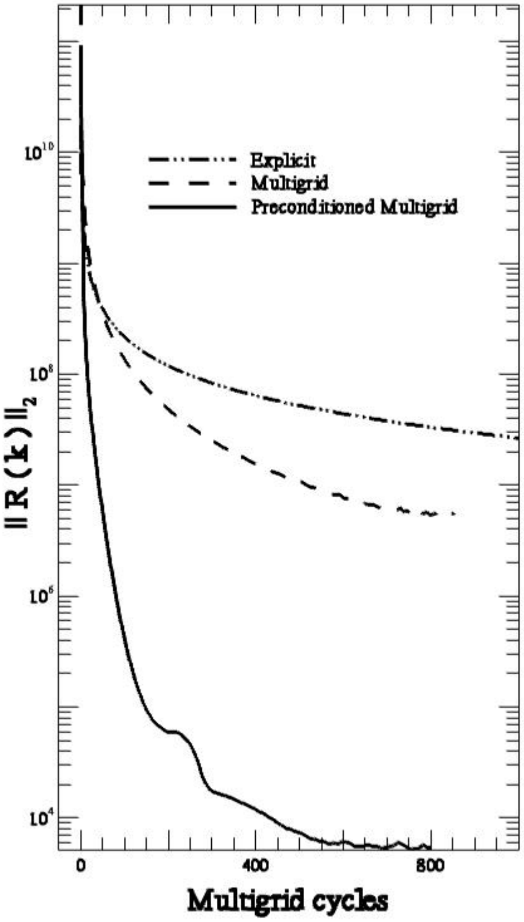

Figure 6: Comparisons of convergence rates as a function of multigrid cycles for 4-level V-cycle multigrid between regular multigrid and preconditioned multigrid with a 5-stage optimal smoothing scheme for the fully-developed turbulent pipe flow.

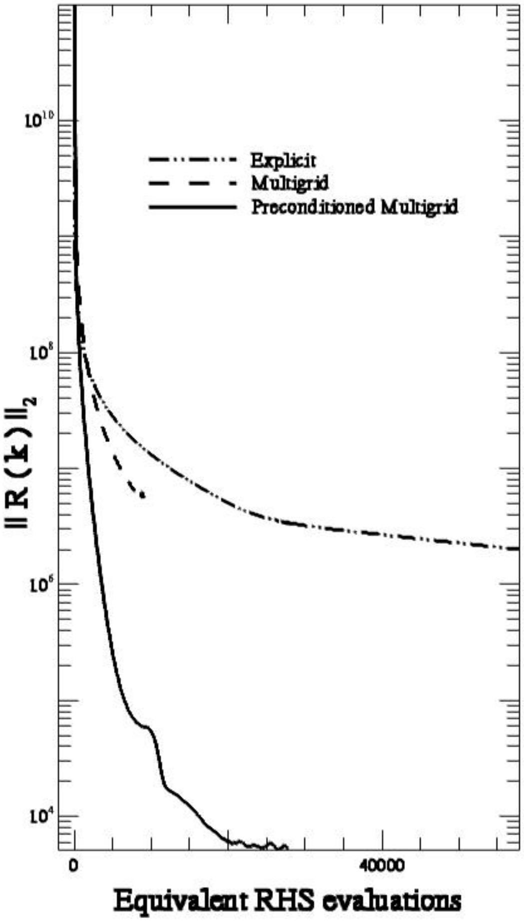

Figure 7: Comparisons of convergence rates as a function of the number of equivalent RHS evaluations for 4-level V-cycle multigrid between regular multigrid and preconditioned multigrid with a 5-stage optimal smoothing scheme for the fully-developed turbulent pipe flow.

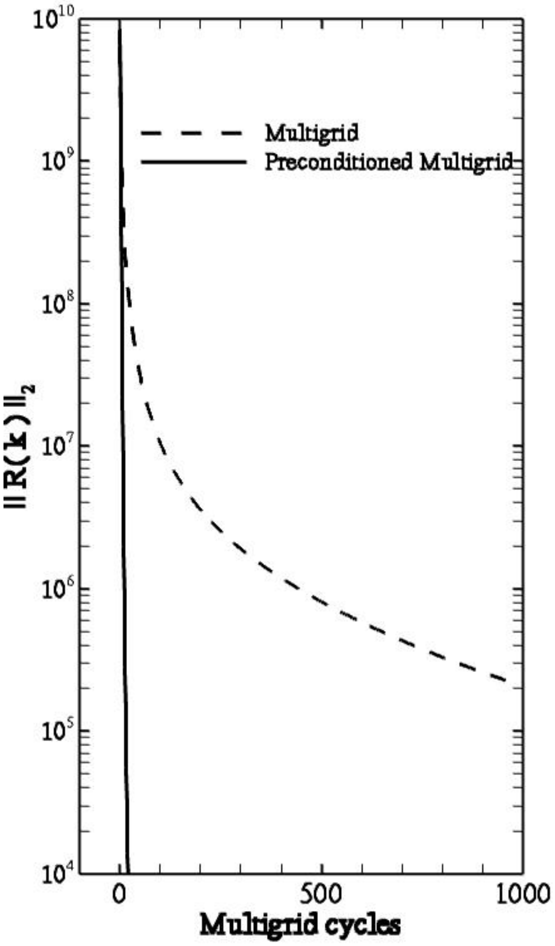

Figure 8: Comparisons of the convergence rates between the preconditioned multigrid and regular multigrid both using 3-level V-cycle with a 5-stage optimal smoothing scheme for the fully-developed turbulent pipe flow.

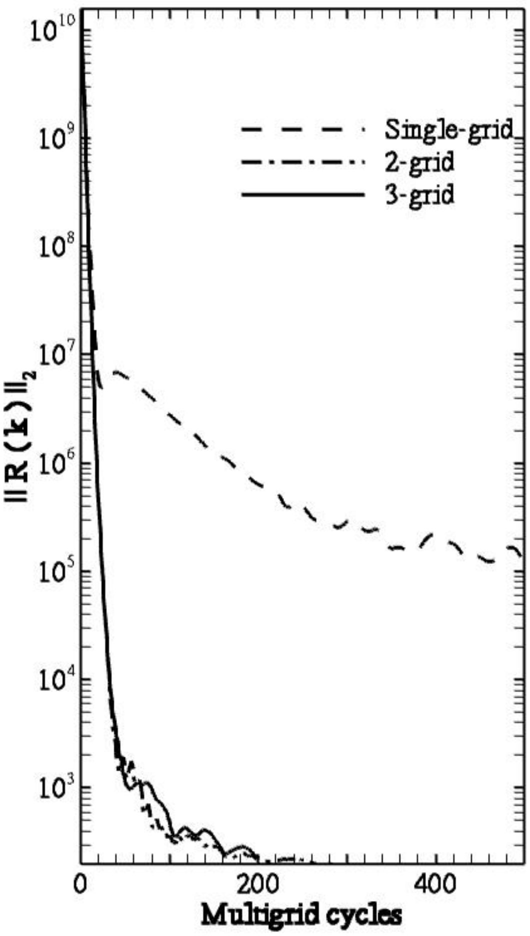

Figure 9: Comparisons between the grid-level effects on convergence of the preco nditioned V-cycle multigrid with a 5-stage optimal smoothing scheme for the fully-developed turbulent pipe flow.

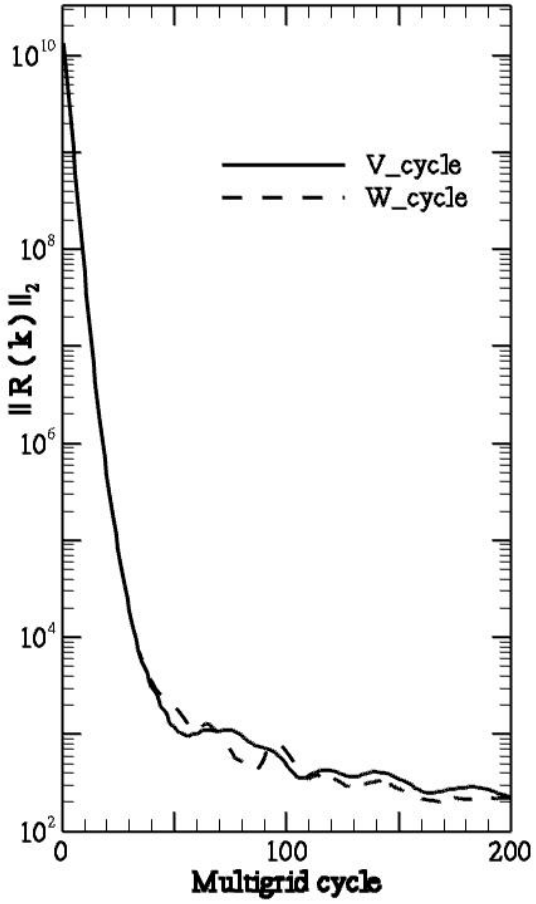

Figure 10: Comparisons between the V- and W-cycle preconditioned multigrid convergence rates of a 3-level preconditioned multigrid with 5-stage optimal smoothing scheme for the fully-developed pipe flow.

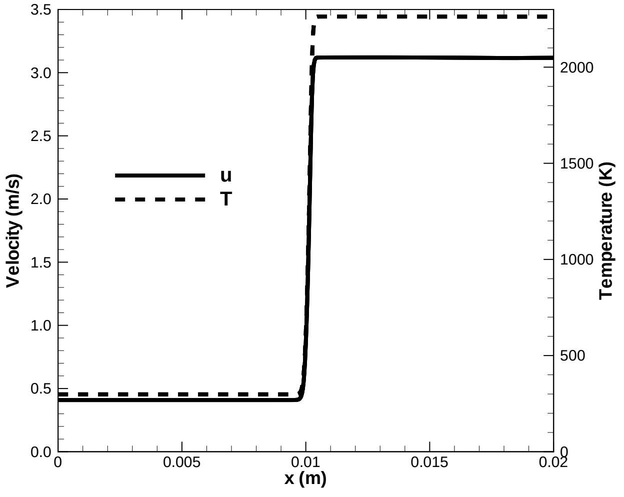

Figure 11: Velocity and Temperature distributions of steady one-dimensional premixed methane-air flame structure for $\phi = 1$.

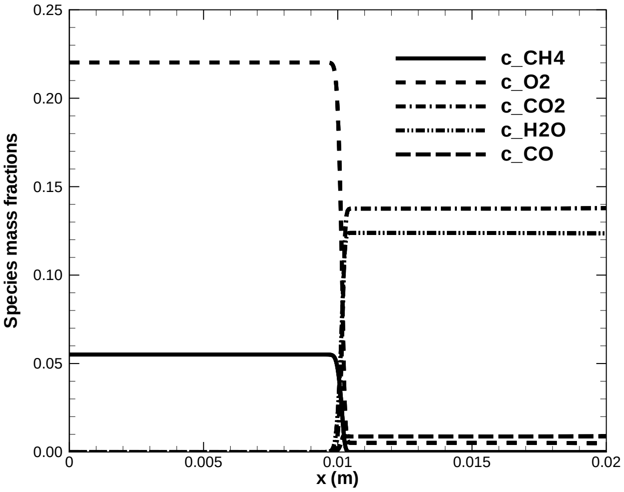

Figure 12: Species mass fraction distributions of steady one-dimensional premixed methane-air flame structure for $\phi = 1$.

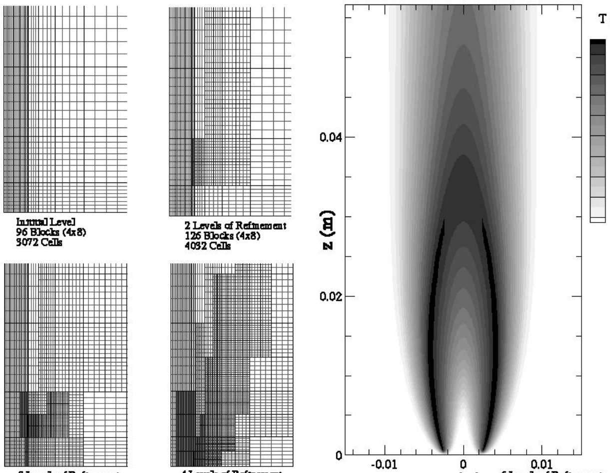

Figure 13: Solution of methane-air axisymmetric laminar diffusion flame showing the computed isotherms and flame structure obtained for a 396 block mesh with 12,672 cells and five levels of refinement. The sequence of adaptively refined grids, showing both the solution blocks and computational cells, is also shown in the figure.

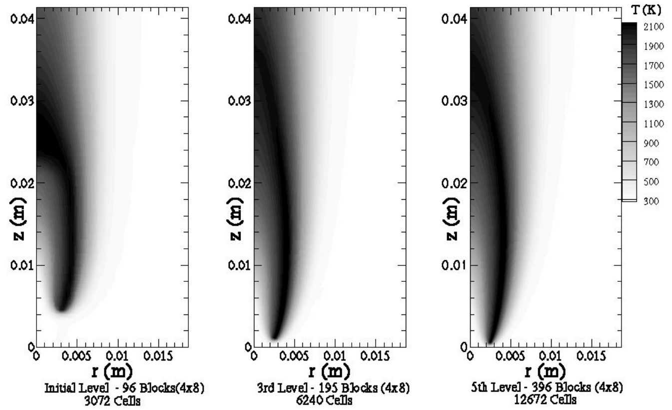

Figure 14: Predicted laminar diffusion flame temperature (K) comparison for 3 different levels of mesh refinement.

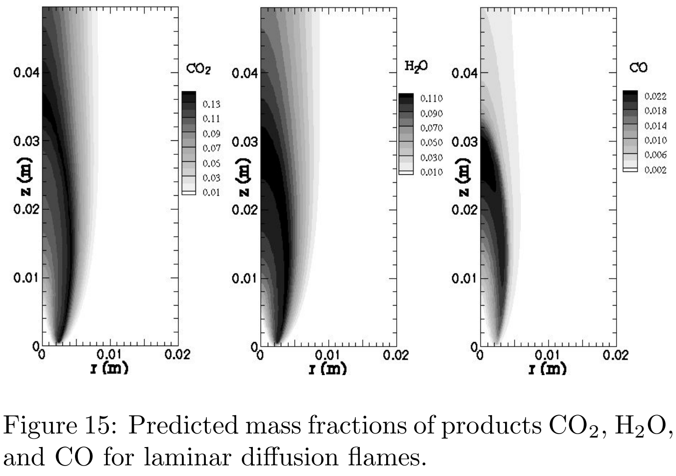

Figure 15: Predicted mass fractions of products CO_2, H_2O, and CO for laminar diffusion flames.

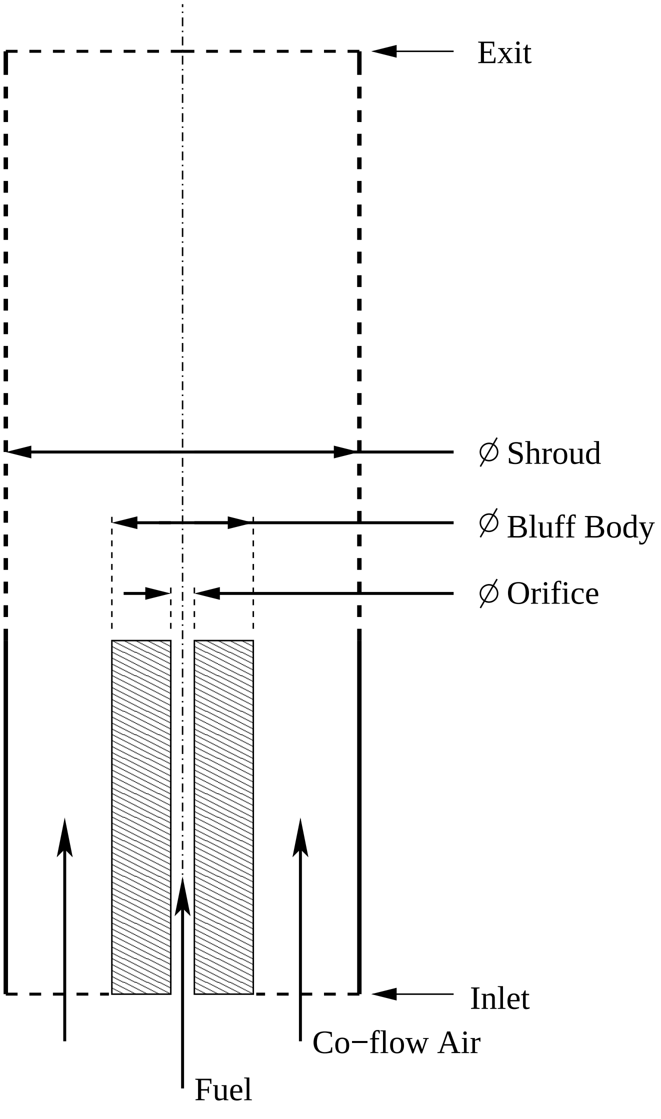

Figure 16: Schematic of the Sydney bluff-body burner showing the fuel jet, co-flow, and bluff-body geometry.

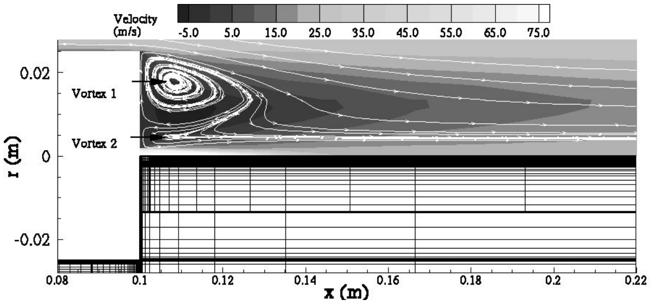

Figure 17: Predicted flow velocity and streamlines for non-reacting flow field of bluff-body burner.

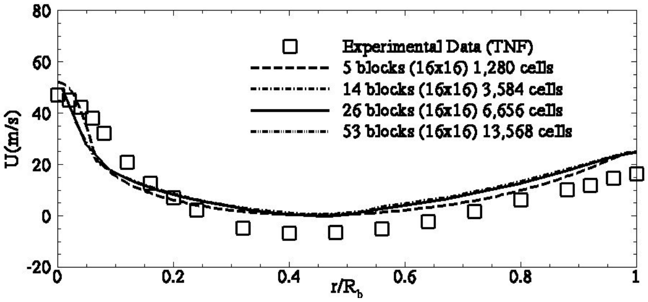

Figure 18: Comparison of predicted and measured axial velocity component at $x/D_b = 0.6$ downstream from the base of the bluff-body for non-reacting bluff-body burner with air jet.

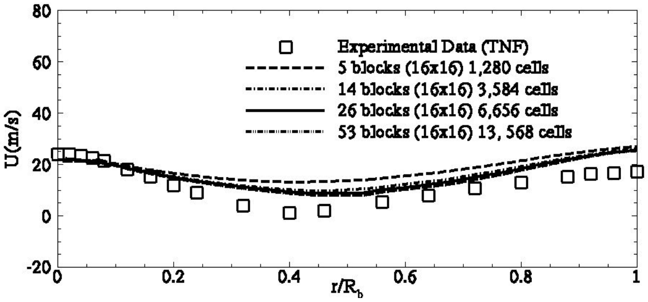

Figure 19: Comparison of predicted and measured axial velocity component at $x/D_b = 1.0$ downstream from the base of the bluff-body for non-reacting bluff-body burner with air jet.

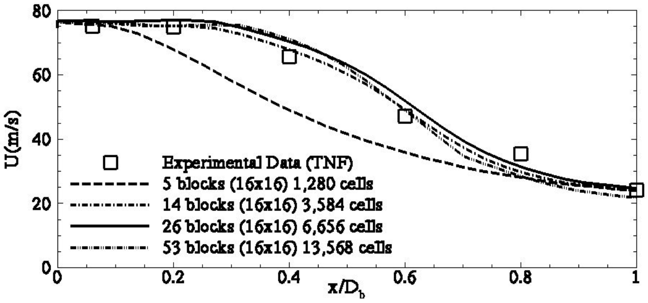

Figure 20: Comparison of predicted and measured on-axis axial profiles of the mean axial velocity component downstream from the base of the bluff-body for non-reacting bluff-body burner with air jet.

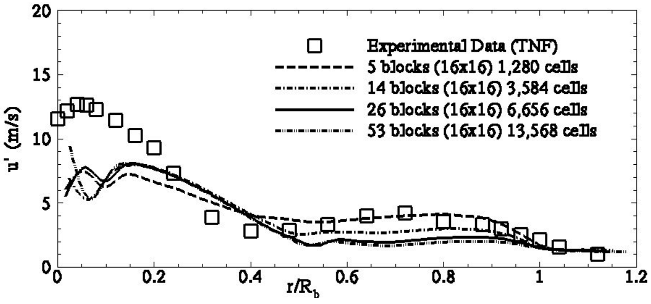

Figure 21: Comparison of predicted and measured $\sqrt{\overline{u'^2}}$ at $x/D_b = 0.6$ downstream from the base of the bluff-body for non-reacting bluff-body burner with air jet.

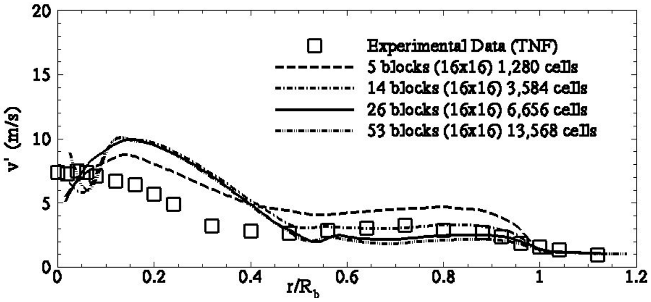

Figure 22: Comparison of predicted and measured $\sqrt{\overline{v'^2}}$ at $x/D_b = 0.6$ downstream from the base of the bluff-body for non-reacting bluff-body burner with air jet.

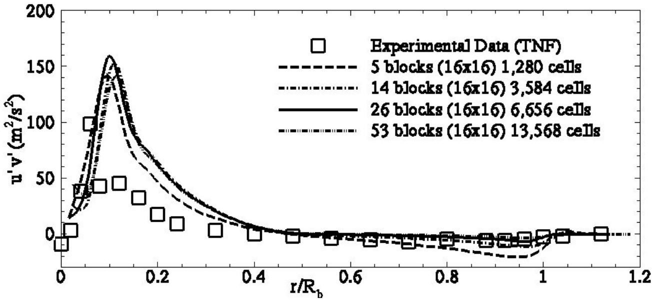

Figure 23: Comparison of predicted and measured $\overline{u'v'}$ at $x/D_b = 0.6$ downstream from the base of the bluff-body for non-reacting bluff-body burner with air jet.

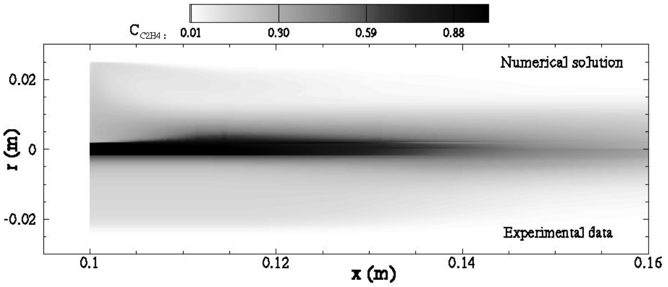

Figure 24: Predicted mean C_2H_4 mass fraction for non-reacting flow field of bluff-body burner.

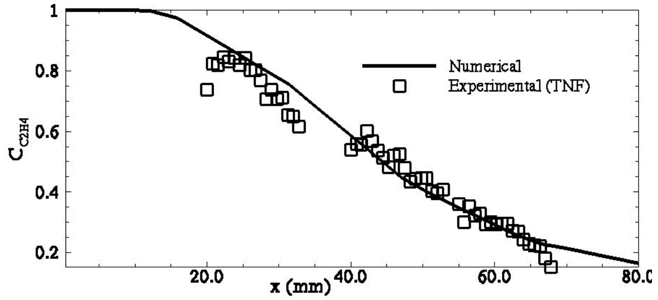

Figure 25: Predicted axial profile of the mean C_2H_4 mass fraction for non-reacting flow field of bluff-body burner.

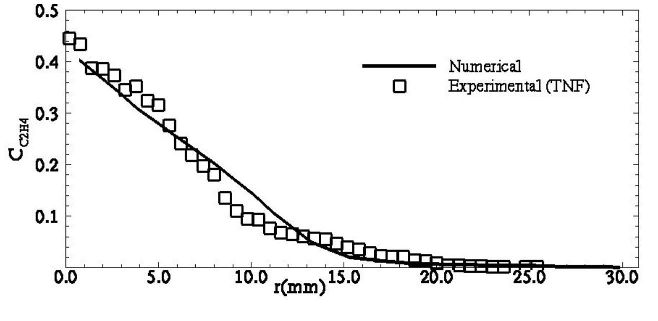

Figure 26: Predicted radial profile of the mean C_2H_4 mass fraction at $x/D_b = 1.0$ for non-reacting flow field of bluff-body burner.

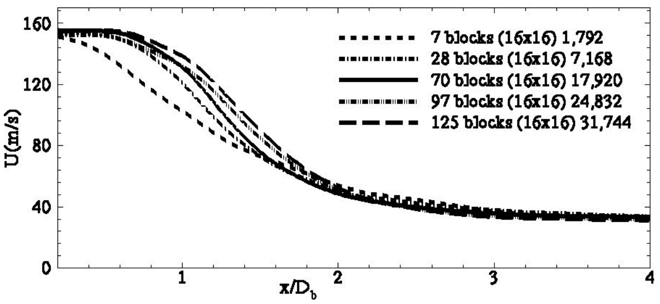

Figure 27: Predicted mean axial velocity along the centerline of the bluff-body for reacting bluff-body burner.

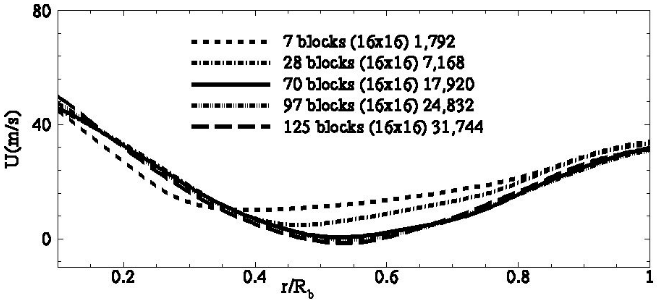

Figure 28: Predicted mean axial velocity at $x/D_b = 1.92$ downstream from the base of the bluff-body for reacting bluff-body burner.

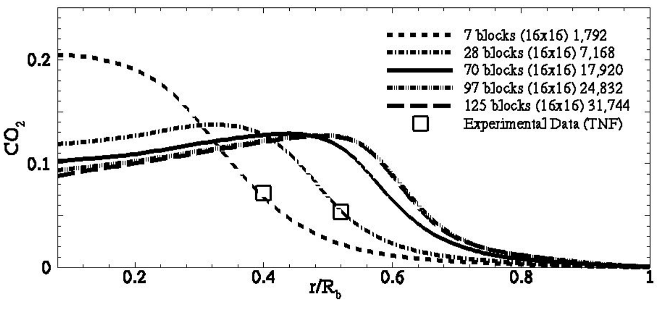

Figure 29: Predicted mass fraction of CO_2 at $x/D_b = 1.92$ downstream from the base of the bluff-body for reacting bluff-body burner.

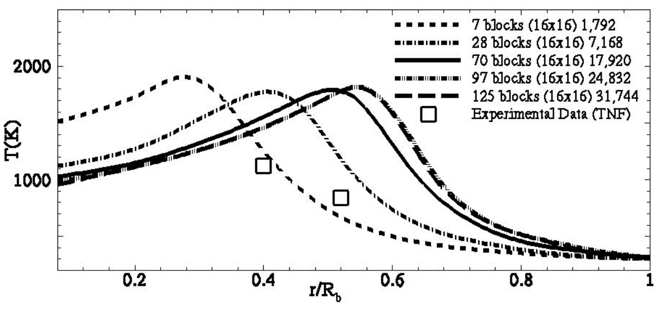

Figure 30: Predicted mass temperature at $x/D_b = 1.92$ downstream from the base of the bluff-body for reacting bluff-body burner.

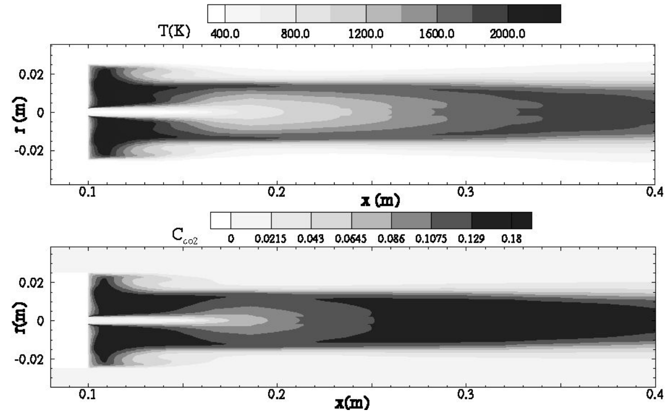

Figure 31: Predicted mean temperature and CO_2 mass fraction for reacting flow field of bluff-body burner.

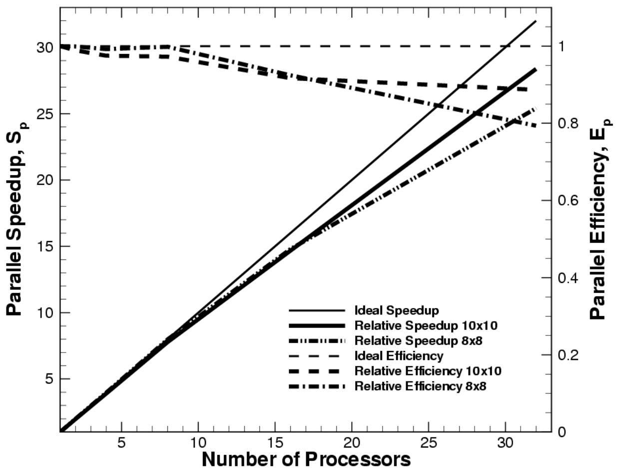

Figure 32: Scaled parallel speed-up and parallel efficiency for a fixed-size laminar diffusion flame problem using up to 32 processors.

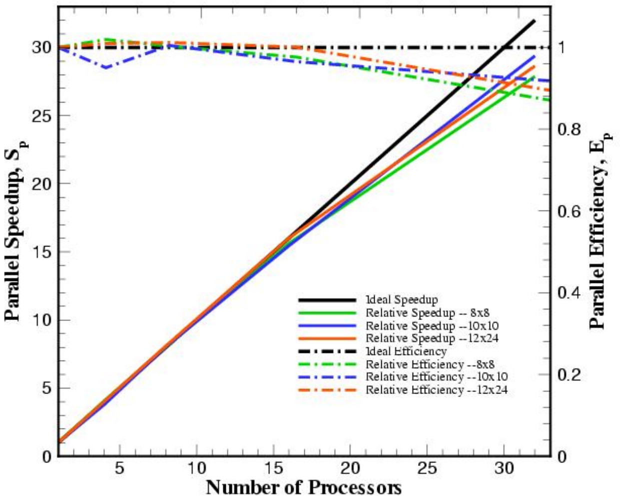

Figure 33: Parallel speedup (strong scaling), S_p and the parallel efficiency, E_p, for a fixed size problem using up to 32 processors.

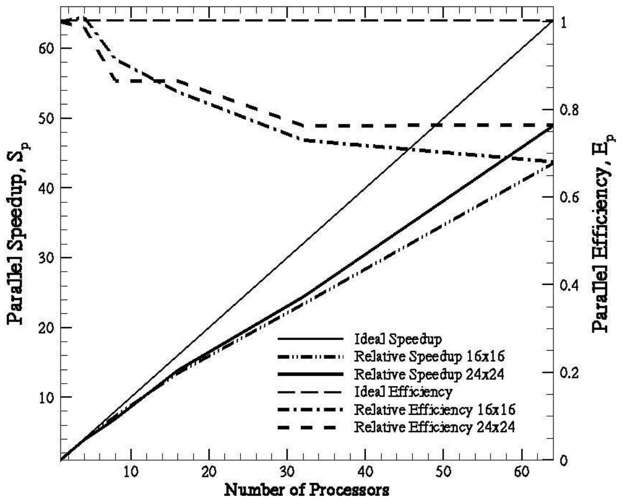

Figure 34: Parallel speedup (strong scaling) and efficiency for computation of a two-dimensional turbulent diffusion flame problem with 3-level V-cycle preconditioned multigrid using up to 64 processors.